

JGR Atmospheres

RESEARCH ARTICLE

10.1029/2018JD029697

Key Points:

- Short-term $\Delta\text{CO}/\Delta\text{CO}_2$ ratios characterized air masses measured by aircraft over South Korea during the 2016 KORUS-AQ field campaign
- The air mass combustion efficiency signature can be assessed with the distribution of the correlated short-term CO to CO₂ slopes
- Differences were found between Chinese influenced and South Korea influenced air masses, which reflect the known sources in each country

Supporting Information:

- Supporting Information S1
- Figure S1
- Figure S2
- Figure S3
- Figure S4
- Figure S5
- Figure S6
- Figure S7
- Figure S8
- Figure S9
- Figure S10
- Figure S11
- Figure S12
- Figure S13

Correspondence to:

H. S. Halliday,
hannah.s.halliday@nasa.gov

Citation:

Halliday, H. S., DiGangi, J. P., Choi, Y., Diskin, G. S., Pusede, S. E., Rana, M., et al. (2019). Using short-term CO/CO₂ ratios to assess air mass differences over the Korean Peninsula during KORUS-AQ. *Journal of Geophysical Research: Atmospheres*, 124, 10,951–10,972. <https://doi.org/10.1029/2018JD029697>

Received 20 SEP 2018

Accepted 1 JUL 2019

Accepted article online 12 July 2019

Published online 23 OCT 2019

Author Contributions:











Conceptualization: J. P. DiGangi

Data curation: J. P. DiGangi, Y. Choi, G. S. Diskin, S. E. Pusede, M. Rana, J. B. Nowak, C. Knote, X. Ren, H. He, R. R. Dickerson, Z. Li

Formal analysis: H. S. Halliday, G. S. Diskin
(continued)

©2019. American Geophysical Union.
All Rights Reserved.

Using Short-Term CO/CO₂ Ratios to Assess Air Mass Differences Over the Korean Peninsula During KORUS-AQ

H. S. Halliday^{1,2} , J. P. DiGangi¹ , Y. Choi^{1,3} , G. S. Diskin¹ , S. E. Pusede⁴, M. Rana^{1,3}, J. B. Nowak¹ , C. Knote⁵ , X. Ren^{6,7} , H. He^{6,8} , R. R. Dickerson^{6,8} , and Z. Li^{6,8,9} 

¹NASA Langley Research Center, Hampton, VA, USA, ²Universities Space Research Association, Columbia, MD, USA, ³Science Systems and Applications, Inc., Hampton, VA, USA, ⁴Department of Environmental Sciences, University of Virginia, Charlottesville, VA, USA, ⁵Meteorological Institute, LMU Munich, Munich, Germany, ⁶Department of Atmospheric and Oceanic Science, University of Maryland, College Park, MD, USA, ⁷NOAA Air Resources Laboratory, College Park, MD, USA, ⁸Earth System Science Interdisciplinary Center, University of Maryland, College Park, MD, USA, ⁹State Key Laboratory of Earth Surface Processes and Resource Ecology, College of Global Change and Earth System Science, Beijing Normal University, Beijing, China

Abstract One-second in situ measurements of CO and CO₂ mole fractions were made aboard the National Aeronautics and Space Administration DC-8 aircraft during the 2016 KORUS-AQ joint air quality and atmospheric chemistry field campaign in South Korea. The ratio of CO to CO₂ enhancement is used to characterize regional combustion source signatures. Calculations of the $\Delta\text{CO}/\Delta\text{CO}_2$ ratio were made with a short duration rolling window (60 s), filtered by the coefficient of determination (R^2), and plotted as distributions to characterize air masses measured from the aircraft during the campaign. The KORUS-AQ sampling domain was divided into analysis regions to facilitate the analysis. Over Seoul, the boundary layer shows a low-ratio signature in the $\Delta\text{CO}/\Delta\text{CO}_2$ ratios, with more than 50% of the correlated slopes in the boundary layer falling below 1% $\Delta\text{CO}/\Delta\text{CO}_2$, and 80% of the slopes between 0% and 2% $\Delta\text{CO}/\Delta\text{CO}_2$. However, this behavior changes to a larger ratio distribution at higher altitudes. The West Sea receptor region was divided into three analysis sectors, by meteorological regime, and used in conjunction with measurements collected over China during the KORUS-AQ campaign time period to characterize the Chinese $\Delta\text{CO}/\Delta\text{CO}_2$ ratio signature. Chinese-type emissions have a slope distribution that is shifted to higher ratios and broadened compared to measurements over Seoul, with the bulk of the measurements between 2% and 4% $\Delta\text{CO}/\Delta\text{CO}_2$, with few negative slopes. The measured ratio trends over South Korea are consistent with inventoried CO and CO₂ emissions.

Plain Language Summary Measurements of carbon monoxide (CO) and carbon dioxide (CO₂) were made over South Korea in May and June of 2016. The ratio of CO to CO₂ provides information about the combustion sources in a region, as most of the CO measured in the atmosphere is sourced from combustion, such as open air fires or engines. Using a 1-s data set, the short-term slopes of CO to CO₂ enhancement were calculated by making a measurement of the CO to CO₂ slope at every observation using the data in the surrounding minute. Plotting the distributions of the short-term slopes with correlated values in the calculation window reveals whether the air masses have mostly low ratios of CO/CO₂, which indicates high-efficiency combustion, or mostly high ratios of CO/CO₂, from low-efficiency combustion. The slope distributions over the Seoul megacity show low-ratio distributions, but at high altitudes the ratios move to higher values, showing that the combustion sources change with altitude and have a less efficient combustion signature. Meanwhile, the ratios that were measured over the West Sea show that the air coming to South Korea from China has higher CO/CO₂ ratios than the air that is measured over South Korea.

1. Introduction

Sustained industrial growth in East Asia since 1970 has resulted in widespread prosperity (Hanushek & Woessmann, 2016; Kimura & Obashi, 2016; Yeon et al., 2016) but has been accompanied by degraded air quality throughout the region, primarily attributed to the increase in power generation and industry (Chan & Yao, 2008; Fang et al., 2009; Streets et al., 2000; Streets & Waldhoff, 2000; van der A et al., 2017; Zhao et al., 2008). East Asia encompasses China, Korea, and Japan, and all of these countries are affected

Funding acquisition: J. P. DiGangi, G. S. Diskin

Investigation: J. P. DiGangi, Y. Choi, G. S. Diskin, S. E. Pusede, M. Rana, C. Knote, X. Ren, H. He, R. R. Dickerson, Z. Li

Methodology: H. S. Halliday, J. P. DiGangi, Y. Choi, G. S. Diskin, J. B. Nowak, C. Knote, X. Ren, H. He, R. R. Dickerson, Z. Li

Project administration: J. P. DiGangi, G. S. Diskin

Resources: J. P. DiGangi, Y. Choi, G. S. Diskin, S. E. Pusede, M. Rana, J. B. Nowak, C. Knote, X. Ren, H. He, R. R. Dickerson, Z. Li

Software: M. Rana

Supervision: J. P. DiGangi, G. S. Diskin

Writing - original draft: H. S. Halliday

Writing - review & editing: H. S. Halliday, J. P. DiGangi, Y. Choi, G. S. Diskin, S. E. Pusede, J. B. Nowak, X. Ren, H. He

by poor air quality with contributions from both local and transboundary pollution. Transboundary air quality issues are a difficult problem for the enforcement of environmental regulations, with emissions policy differing between localities and nations.

The Korean Peninsula is susceptible to pollution transport from international sources, and studies have found evidence of Chinese sources impacting the air quality in Korea over different areas, sampling regimes, and time periods (Han et al., 2008; Heo et al., 2009; Kim et al., 2016; Koo et al., 2008; Lee et al., 2013; Oh et al., 2015; Park et al., 2004). While South Korea has implemented control strategies to improve air quality (Ghim et al., 2005; Kang et al., 2006; Kim & Shon, 2011), there are still poor air quality events, especially in the densely populated Seoul metropolitan region, which is home to approximately 25 million people, 10 million of whom live within the Seoul urban boundary (Kang et al., 2004; Kang et al., 2006; Kim et al., 2007; Kim et al., 2014; Lee et al., 2013). Metrics for determining the underlying contributions to severe air quality events are critical tools for policymakers to determine effective mitigation strategies.

The atmospheric ratio between carbon monoxide (CO) and carbon dioxide (CO₂) can be used as a tracer for source combustion efficiency, as these two species generally have common combustion sources with specific emission ratios (Ward et al., 1996). CO has an OH oxidation lifetime of approximately 2 months, making it a good tracer for synoptic-scale transport yet is also not long enough lived to have high stable background levels (Heald et al., 2003; Liu et al., 2003; Staudt et al., 2001; Vay et al., 2011). CO is predominantly produced by incomplete combustion of carbon-containing fuel, with typically minor contributions from the oxidation of atmospheric hydrocarbons (Bakwin et al., 1995; Potosnak et al., 1999). During high-efficiency combustion (e.g., modern power plants) fuel carbon is converted to CO₂ with nearly perfect efficiency, producing extremely low ratios of CO to CO₂ (<0.1% CO/CO₂). Conversely, low-efficiency combustion from cold or smoldering processes, or from low-efficiency engines, will produce large amounts of CO. The lowest efficiency processes, like biomass burning, yield ratios over 10% CO/CO₂ (Andreae & Merlet, 2001; Wang et al., 2010).

Vehicle emissions are a significant source of CO globally (Zhong et al., 2017), but the combustion efficiency of the engines varies widely with both the type and size of the engine and the operating conditions (Tong et al., 2000), in addition to emissions control equipment and engine maintenance. Globally, vehicle combustion efficiency has increased with time as compliance with emissions standards has improved (Popa et al., 2014; Singer & Harley, 1996), but standards vary between countries (Huo et al., 2011). South Korea has generally had stronger vehicle emissions standards than China (Wang et al., 2014), although combustion efficiency has been increasing in China with improved emissions control technology and government incentivized implementation of improved standards (Zhang et al., 2009; Zheng et al., 2018).

The atmospheric ratio between CO and CO₂ has been used extensively to characterize regional source signatures (Newman et al., 2013; Silva et al., 2013; Suntharalingam et al., 2004; Turnbull, Tans, et al., 2011; Vay et al., 2011; Wang et al., 2010). Studies in East Asia have found regional and seasonal changes in this ratio that are attributable to changes in heating and vehicle use (Han et al., 2009; Wang et al., 2010). Silva et al. (2013) used satellite retrievals to assess CO/CO₂ ratios over megacities as an assessment of anthropogenic emissions and found that the CO/CO₂ ratios were lower over the Seoul megacity than over cities in China (Beijing and Shanghai) and Japan (Tokyo and Osaka/Kobe), with values that agreed with Japanese and Chinese outflow reported in Suntharalingam et al. (2004) and Turnbull, Tans, et al. (2011). The downside to using a total air mass CO/CO₂ ratio is that the ratio will be the sum of all constituent combustion sources and sinks within an analysis region (Suntharalingam et al., 2004; Vay et al., 2011). While useful for assessing an overall outflow source signature, an overall ratio has limited information value. By examining the distributions of short-term continuous slopes, we create regional fingerprints that can be used to assess emissions and mixing behavior between analysis regions, giving us greater insight into the mix of local sources and transport.

To investigate the characteristics of air masses observed during KORUS-AQ, this work uses the in situ enhancement ratio of CO to CO₂ measured on the National Aeronautics and Space Administration (NASA) DC-8 aircraft. This paper presents a method for calculating short-term CO/CO₂ ratios using high time resolution aircraft data and uses these short-term ratios to characterize the distributions of slopes and compare these slope distributions by analysis region. We present the method, show a breakdown of the KORUS-AQ data by general analysis region, then examine how these slope distributions change between

the boundary layer and the free troposphere by using vertical binning of the dataset. To get a better understanding of the behavior of the short-term slopes, we use the West Sea as a receptor location and characterize the incoming air masses from China and compare the KORUS-AQ results to an in situ data set that was collected over mainland China during the KORUS-AQ time frame. Finally, we compare the short-term slope distribution results to a Korean emissions inventory.

2. Data and Methods

2.1. KORUS-AQ Field Campaign and In Situ Aircraft Measurements

KORUS-AQ was an international joint air quality and atmospheric chemistry field campaign conducted with coordinated measurements by U.S. and Korean scientists onboard the NASA DC-8 aircraft, with additional information from ground sites. Atmospheric composition data were collected during 20 science flights conducted between 1 May 2016 and 9 June 2016, ranging primarily throughout the southern Korean Peninsula and West Sea. The aircraft payload included a wide range of instruments for measuring gas-phase chemical species and particulate chemical and physical properties. CO₂ was measured via non-dispersive infrared spectroscopy using a modified LICOR 6252 instrument with both a precision and an accuracy of 0.13 ppm (Vay et al., 2003). CO was measured via wavelength modulation spectroscopy using the DACOM instrument suite with a precision of 0.4 ppb and an accuracy of 2% of the measurement (Sachse et al., 1987, 1991). Both instruments were calibrated in flight using standards assayed by the Global Monitoring Division of the National Oceanic and Atmospheric Administration Earth System Research Laboratory and traceable to World Meteorological Organization scales x2007 (CO₂) and x2014A (CO).

Three analysis regions are defined for the measurements collected over South Korea during KORUS-AQ, which are shown in Figure 1. The three regions are the Seoul Megacity region, the general South Korean Peninsula, and the Yellow Sea (referred to in this study as the West Sea). These boundaries are found on the KORUS-AQ data archive and are publicly available, along with all other data included in this work (<https://www-air.larc.nasa.gov/missions/korus-aq/> website; KORUS-AQ Science Team, 2018).

The Seoul region targets the Seoul megacity, allowing the assessment of emissions by and impacts on the primary population center of South Korea. The Peninsula region characterizes the mixed-use landscape over South Korea and a small portion of Southern Japan and the Sea of Japan. The Peninsula region excludes Seoul. The West Sea region covers measurements taken over the Yellow Sea, which is usually upwind of the Korean Peninsula. West Sea air masses have been sampled in the past to quantify transboundary pollution in East Asia (Chung & Kim, 2008; Suntharalingam et al., 2004). In addition to the three major South Korean analysis regions, the West Sea has also been divided into three analysis sectors, also shown in Figure 1. These three sectors are Sector A, the Korean and Seoul outflow; Sector B, a mix of inflow and outflow to South Korea; and Sector C, which is only inflow to the South Korean Peninsula.

2.2. Chinese Data In Situ Measurements

The measurement location in China is shown in Figure 1, in relation to the flight tracks of the DC-8 during KORUS-AQ. Aircraft measurements were made using a Chinese Y-12 IV, a high wing, twin-engine, turbo-prop aircraft (similar to a DeHavilland Twin Otter) equipped with meteorological and chemical instruments. Concentrations of methane (CH₄), CO₂, CO, and water vapor were made with a four-channel Picarro cavity ring-down spectrometer (Model G2401-m) at a frequency of 0.5 Hz. Ambient air from the nose of the aircraft was pulled through a rear-facing PFA Teflon inlet tube (O.D. = 0.95 cm and I. D. = 0.64 cm) at a total flow rate of 10 L/min (equivalent to a ~0.7-s residence time in the sample line). The Picarro was calibrated with CO₂/CH₄/CO standards certified at National Institute of Standards and Technology. The measurement precisions for 1-min data were 0.04 ppm for CO₂, 9 ppb for CO, and 0.4 ppb for CH₄ (standard deviations [1σ] of 0.5-Hz data over 5 min).

2.3. Wind Cross Back Trajectory Analysis

The FLEXible PARTicle Dispersion Model (FLEXPART; Stohl et al., 2005) has been used to calculate air mass origin by means of back trajectories (Seibert & Frank, 2004). For this, 6-hourly analyses (interlaced with 3-hr forecasts) of the National Centers for Environmental Prediction Global Forecasting System at 0.25° horizontal resolution have been used as meteorological driver. Back trajectories were calculated from the

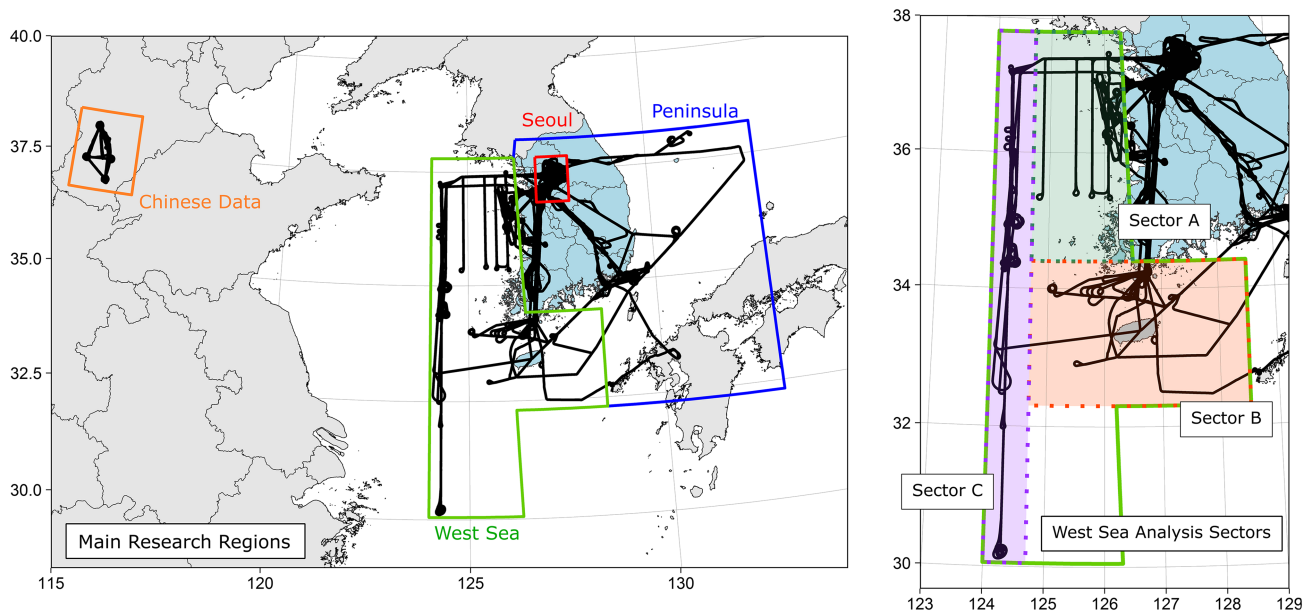


Figure 1. Flight paths for all flights used in this study, and the associated regional analysis boundaries. The left map shows the flight paths for the 20 KORUS-AQ science flights, overlaid with the three South Korean analysis region boundaries used in this study. Three general analysis regions are used: Seoul (red), which targets the urban emissions from the Seoul Metropolitan area; the Peninsula (blue), which covers the mixed-use environment outside of Seoul; and the West Sea (green), measurements over the Yellow Sea that can be used as a receptor location for inflow/outflow from the Korean Peninsula. The Chinese science flights are boxed in orange and show the flight paths of the 11 flights undertaken during the Chinese subcampaign. The right map shows the three West Sea analysis sectors. Sector A, Korean outflow (green); Sector B, mixed Korean inflow/outflow (red-orange); and Sector C, Korean inflow (purple).

position of NASA DC-8 in 1-min intervals during a research flight, emitting 10,000 particles every time. Processes like convection or turbulence then act stochastically on these particles. Cluster analysis (Stohl et al., 2002) was used to summarize the particle positions into five center locations at hourly intervals back in time.

This paper focuses on general behavior over different regions. To simplify the analysis of the back trajectories, the results use wind cross summary plots of the FLEXPART back trajectories. The back trajectories associated with a particular target region are identified by the latitudes and longitudes of their terminal points on the flight track (the “release positions”). For the selected back trajectories associated with a particular geographic region, the latitudes and longitudes are treated separately. The statistics (the percentiles) of all latitudes for the target area are calculated separately from the longitudes, treating the two variables as pseudo-independent. The two groups are plotted as lines on the map, crossing at the median latitude and longitude. This creates a wind cross, describing the bulk behavior of the trajectories terminating within a defined area.

Figure 2 shows how the wind cross simplifies and clarifies the wind trajectory plot for 9 May 2016, as well as a schematic for interpreting the wind cross. The wind crosses use the 10th, 25th, 50th, 75th, and 90th percentiles to describe the behavior of 80% of the back trajectories initiated within an analysis region. The wind crosses are separated by back trajectory hour, using -12 , -24 , -36 , and -48 hr to show how the bulk behavior of the back trajectories changes with time, going back 2 days. The latitude/longitude polygon defined by the solid lines will show where the center 50% of the back trajectories were at a given back trajectory hour, and the polygon defined by the dotted lines show the center 80% of the back trajectories for the same hour.

2.4. Boundary Layer Height Calculation

Boundary layer heights were calculated from the aircraft vertical profiles using a technique outlined in Martins et al. (2012) and Halliday et al. (2016), based on Seidel et al. (2010). The 222 tagged vertical profiles in the KORUS-AQ data set were averaged to 50-m vertical bins, and the potential temperature lapse rate ($\Delta\theta/\Delta z$) and the change in relative humidity (ΔRH) were calculated for each bin. The boundary layer (BL) was

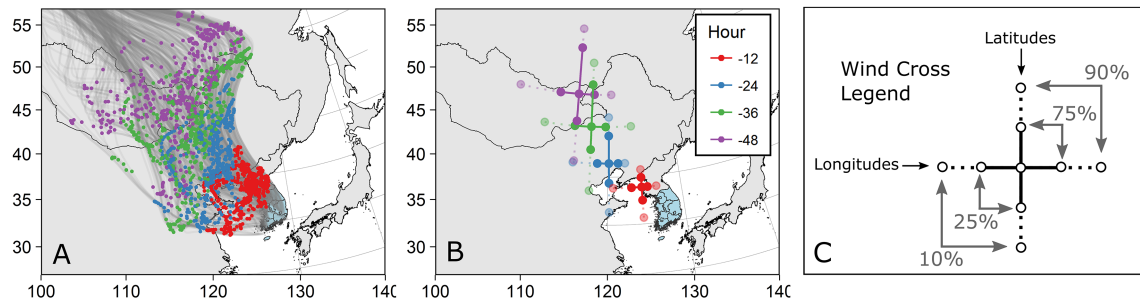


Figure 2. Defining the wind cross summary graphic. These sample maps were constructed from the 9 May 2016 DC-8 aircraft flight. For all FLEXPART back trajectories originating within a specified geographic region (a), percentiles are calculated from the latitudes and longitudes at set back trajectory hours. The crosses are constructed for each included hour by crossing the percentiles at the median latitude and longitude (50th percentile), with the inner cross constructed from the 25th and 75th percentiles, and the outer cross constructed from the 10th and 90th percentiles (b). The full cross shows the area that 80% of the calculated back trajectories travel through at a specified back trajectory time; the inner cross shows the area traveled through by the inner 50% of the back trajectories (c).

defined as a layer with a potential temperature lapse rate ≥ 6 K/km, and a Δ RH from the top of the layer to the bottom of the layer $\leq -5\%$ RH. If multiple layers were picked with these metrics, the layer with the greatest Δ RH was selected, with a hard maximum boundary layer height of 3.5 km. Each profile was inspected visually to check the BL assignment; two flights with weaker boundary layer gradients, 21 May 2016 and 1 June 2016, used a minimum potential temperature lapse rate of 5 K/km to pick out the appropriate inversions. In a small subset of the profiles, well mixed residual layers or water vapor layers cause the water vapor metric to incorrectly assign the BL height. These profiles were identified with a visual inspection, and in eight cases the boundary layer was assigned to the layer with the largest lapse rate rather than the largest Δ RH. The boundary layer height was interpolated linearly between calculated BL height points, and this interpolated line was used to define a boundary layer tag for the data.

The boundary layer heights for the Chinese data set were calculated with the same technique, using a 25-m bin. A ≥ 5 K/km potential temperature lapse rate was used, and a Δ H₂O mixing ratio ≤ -100 ppm (measured by the Picarro instrument) over the layer defined potential boundary layer heights, with the boundary with the largest water vapor difference and a hard altitude limit of 3 km selected. Three flights used the aircraft instrument measurement of RH, due to loss of water mole fraction data from the Picarro instrument, 19 May 2016 and the two sorties on 28 May 2016. For these flights, a Δ RH of $\leq -2\%$ RH was used to define the boundary layer height.

Once tagged as boundary layer or free tropospheric, the data were binned vertically by these altitude tags. In the KORUS-AQ data the free tropospheric data were split into a low free tropospheric bin, for free tropospheric measurements below 3 km above sea level (ASL; measured with the pressure altitude), and a high free tropospheric bin for measurements collected equal to or higher than 3 km ASL (see supporting information).

2.5. Short-Term Rolling Δ CO/ Δ CO₂ Calculation Method Description

The short-term slopes between CO and CO₂ are calculated with a centered 1-min rolling window and filtered by the correlation of determination (R^2) to return a slope distribution that provides information about the instantaneous ratios between the two species.

The slopes for the CO to CO₂ relationships (Δ CO/ Δ CO₂) are calculated using the error-adjusted bivariate regression, which accounts for errors on both the x and y axes, detailed in York et al. (2004) and Cantrell (2008), weighting each observation by the total uncertainties (combined pointwise accuracy and precision). Treating the variances symmetrically returns a robust calculation of the Δ CO/ Δ CO₂ relationship that is invariant to exchange of x and y (Cantrell, 2008). This work uses a time-centered 60-s rolling window, defined by time stamps for a maximum of 61 observations in each calculation, and a coefficient of determination cutoff of $R^2 \geq 0.5$. Slope calculations with a R^2 below this cutoff value are considered to be effectively uncorrelated and are not included in the analysis. Additionally, the minimum number of points for a valid slope is set at 3, and slopes that have a Δ CO or Δ CO₂ < 5 times the precision value are dropped to prevent inclusion of slopes that could be driven by noise rather than real covariance. This provides a robust, simple calculation of

Table 1

Percentiles and Mean Value of the Calculated Standard Uncertainties in the Short-Term Slopes

R^2	0%	25%	50%	75%	100%	Mean
<0.5	4.8×10^{-6}	6.2×10^{-4}	0.0012	0.0037	1.8×10^7	116.8
>0.5	1.1×10^{-14}	3.7×10^{-4}	7.3×10^{-4}	0.0014	0.245	0.0012

Note. The uncertainties are in units of per parts per million.

continuous $\Delta\text{CO}/\Delta\text{CO}_2$ slopes over 20 science flights. Additional details on the characterization of the method can be found in the supporting information.

The calculation of the slopes includes a calculation of the slope uncertainty, detailed in York et al. (2004) and Cantrell (2008). For the assessments of the slopes we use the weighted standard error from Cantrell (2008), which adjusts the calculated uncertainties by a “goodness of fit” parameter. In this formulation of the slope uncertainty the calculation is driven by the values and uncertainties on the x axis, which gives the uncertainties units of per parts per million. Table 1 summarizes the standard errors in the slopes for the data, separated by correlated and uncorrelated slopes. We consider the uncertainties in the correlated slopes sufficiently small that we did not filter based on the calculated uncertainties.

There are two major benefits to using these short-term calculations of the $\Delta\text{CO}/\Delta\text{CO}_2$ ratios. First, because this method uses the mole fraction deltas over short time periods we do not need to consider the background of the concentrations. Removing a background value will only change the offset, not the ratio. The delta notation for the slopes is used because the short-term slopes are driven by the change in mole fraction over the calculation window, rather than an enhancement over a background. Second, correlation filtering allows the method to spotlight regions of correlated behavior, such as plumes and air mass boundaries. The slopes are a measurement of the mixing between two air masses and allows the identification and characterization of periods where there are short-term changes in the chemical characteristics of the measured air, such as the nearfield emission signature of $\Delta\text{CO}/\Delta\text{CO}_2$, or the advection of coherent plumes into an analysis region. This is useful in regions with spatially heterogeneous emissions (e.g., China vs. South Korea). Periods of time when the concentrations of the two species are steady in time, and thus uncorrelated during the short time period of the rolling window, are not included in the analysis.

Figure 3 presents the results of applying this method to the 20 science flights in the KORUS-AQ data set, with Figure 3a showing the results of the CO to CO_2 regression for all 20 science flights from KORUS-AQ.

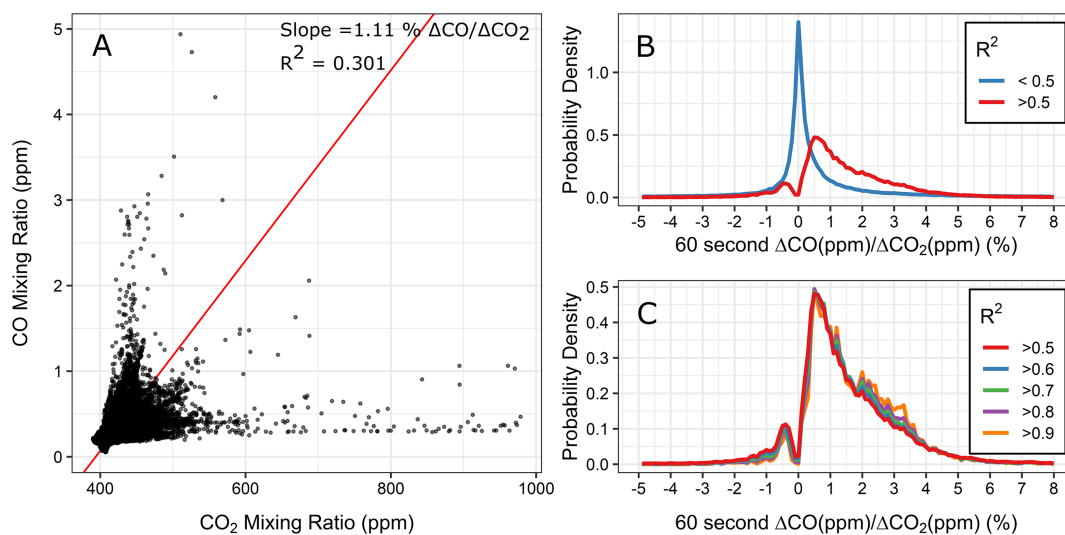


Figure 3. Campaign correlations between CO and CO_2 over the 20 KORUS science flights. (a) The full campaign scatter plot between CO and CO_2 with the error-adjusted bivariate correlation. (b) The slope distributions for the 20 science flights, showing the distributions of the effectively correlated slopes ($R^2 \geq 0.5$), and the effectively uncorrelated slopes ($R^2 < 0.5$). Both lines are normalized to a probability density. (c) The normalized probability distributions of the correlated data, separated by minimum R^2 value. All five R^2 cutoffs yield the same bulk distribution of slopes.

Figure 3b shows the results from the rolling correlation calculations on the same KORUS-AQ data shown in Figure 3a, showing the distribution of slopes calculated over all science flights separated by minimum slope R^2 value. The slopes are reported as percentage values, with the percentage calculated from the slope (ΔCO [ppm]/ ΔCO_2 [ppm]) multiplied by 100. All slope distributions are binned by 0.1% $\Delta\text{CO}/\Delta\text{CO}_2$. Figure 3c presents the normalized distributions of the correlated slopes, separated by minimum R^2 cutoff. The five R^2 cutoff lines collapse to a single normalized distribution, showing that the shape of the slope distributions are not sensitive to the R^2 cutoff. The normalized distributions can be compared on a common scale, without needing to account for sample size differences in the total counts of a distribution.

Over the full campaign the overall regression between CO and CO₂ for the all observations has a slope of 1.1% $\Delta\text{CO}/\Delta\text{CO}_2$ (Figure 3a), but the relationship over all measurements is too uncorrelated ($R^2 = 0.301$) to make any conclusions about the chemical behavior over the full data set. However, the short-term correlations provide additional important information—over all observations, the most commonly observed short-term correlated slope is 0.5% $\Delta\text{CO}/\Delta\text{CO}_2$, and most of the slopes fall between -2% and 4% $\Delta\text{CO}/\Delta\text{CO}_2$. The slope distributions also indicate that there are nonnegligible instances of negative slopes, due to depletions in CO₂ concentration.

The distributions of these slopes coupled with a correlation filter are a simple and powerful way to collect information about the most common correlated instantaneous ratios observed during the campaign. The same correlated ratio must be sampled many times to produce a significant bump in the distributions, and the statistics provide confidence in classifying the distributions as a primarily high ratio signal versus a primarily low ratio signal. Examining how a distribution changes between sampling regions can provide insight to the change in emissions and air masses between the regions.

3. Results

3.1. $\Delta\text{CO}/\Delta\text{CO}_2$ Slope Distributions by Analysis Region

Figure 4 shows the correlated slope distributions by KORUS-AQ analysis region (see Figure 1 for delineation of the regions). All three analysis regions show distributions that peak below 1% $\Delta\text{CO}/\Delta\text{CO}_2$, but the shapes of the distributions indicate source differences between the regions. All three regions have at least 90% of their slopes below 5% $\Delta\text{CO}/\Delta\text{CO}_2$, but the slopes shift to higher values and the distributions become flatter as we move outward from Seoul to the Peninsula and the West Sea analysis regions.

The Seoul distribution is the narrowest in the positive slopes and also has more negative slopes (11.5% of total slopes). Negative slopes between CO and CO₂ are generally interpreted as a signature of biogenic activity, with a loss of CO₂ due to uptake during photosynthesis (Silva et al., 2013; Turnbull, Karion, et al., 2011). The Peninsula region contains fewer correlated negative slopes, and a positive slope distribution with slightly higher ratios compared to the Seoul region. The West Sea analysis region has a slope distribution that is again shifted and broadened compared to the other two regions with higher ratios of $\Delta\text{CO}/\Delta\text{CO}_2$ values. Figure 4b quantifies the percentages of correlated slopes that fall within each $\Delta\text{CO}/\Delta\text{CO}_2$ ratio range. The results from these three regions agree with the observed and modeled $\Delta\text{CO}/\Delta\text{CO}_2$ values in Tang et al. (2018), which assessed the Copernicus Atmosphere Monitoring Service CO and CO₂ forecasts.

Figure 5 summarizes the dynamic ranges for the slopes shown in Figure 4, showing the range of the calculated 60-s ΔCO and ΔCO_2 for the correlated slopes used in the analysis, separated by analysis region. All three regions have increasing ΔCO values with increasing ratio range, showing a larger dynamic range in CO for higher ratios of $\Delta\text{CO}/\Delta\text{CO}_2$. In contrast, in the positive slopes the ΔCO_2 has the opposite behavior, with the highest ΔCO_2 values associated with the low-ratio bin, and the ΔCO_2 mole fractions falling with ratio range. Both species have the smallest dynamic ranges for negative slopes. While the slope distributions show changes in the ratio distributions between regions, the consistent behavior in the dynamic ranges indicates that the underlying behavior in the slope calculations over the different ratio ranges (changes in CO or changes in CO₂) is consistent across the sampling region.

One of the goals of this analysis is to investigate the differences between the Seoul and the West Sea analysis regions to determine if the difference in the slope distributions is connected to emissions differences between South Korea and China. Figure 5 shows that all three analysis regions have the same underlying chemical

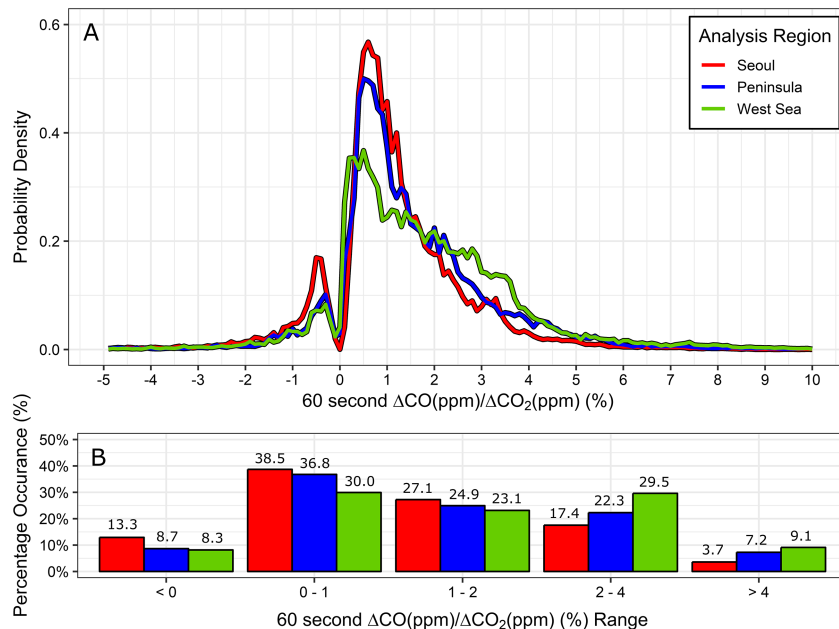


Figure 4. (a) Slope distributions for the full set of science flights organized by analysis regions (Figure 1). The slope distributions are constructed using the $R^2 \geq 0.5$ lines and a 60-s rolling window. (b) Quantification of the distributions by $\Delta\text{CO}/\Delta\text{CO}_2$ ratio range, that is, $<0\%$ $\Delta\text{CO}/\Delta\text{CO}_2$ and $0-1\%$ $\Delta\text{CO}/\Delta\text{CO}_2$. Each bar is colored by analysis region and labeled with the percentage of the distribution that occurs within the listed range.

behavior for the $\Delta\text{CO}/\Delta\text{CO}_2$ ratio ranges. The shift in the distributions between Seoul and the West Sea indicate that there is some difference in the combustion efficiency type between the air mass source regions.

3.2. Seoul Region: Vertical Analysis

An objective of the KORUS-AQ field campaign was to collect a large number of observations over Seoul, typically doing three vertical profiles via missed approaches over the city each flight day. These profiles over Seoul provide good statistics for examining how the ratios behaved over the Seoul analysis region during the campaign. Figure 6 shows the results for the Seoul analysis region when split vertically into the three vertical bins: the boundary layer, the low free troposphere (<3 km ASL), and the high free troposphere (≥ 3 km

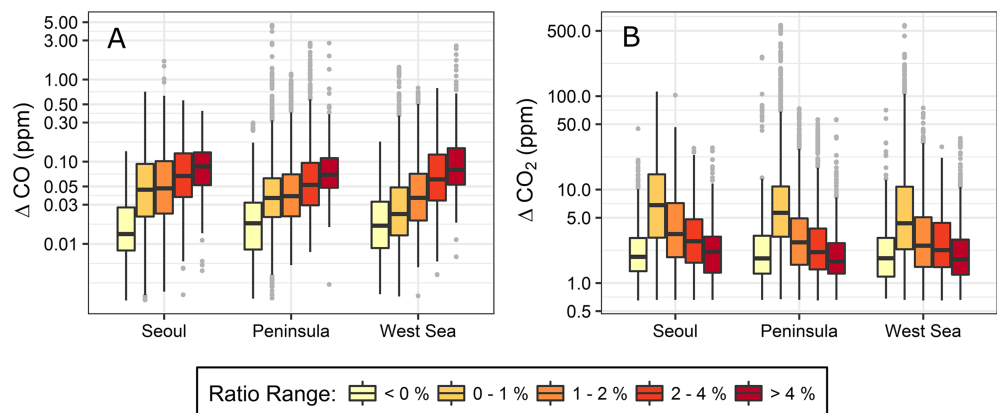


Figure 5. Sixty-second window ΔCO and ΔCO_2 values for each correlated ($R^2 \geq 0.5$) slope, grouped by analysis region (Figure 1) and colored by $\Delta\text{CO}/\Delta\text{CO}_2$ ratio range. Each box and whisker plot shows the 25th, 50th, and 75th percentiles; the whiskers terminate at the last observation within 1.5 times the interquartile range, and all other observations are indicated with outlier points. (a) The ΔCO values for all correlated slopes. (b) The ΔCO_2 values for all correlated slopes. Both subplots are plotted with logarithmic axes.

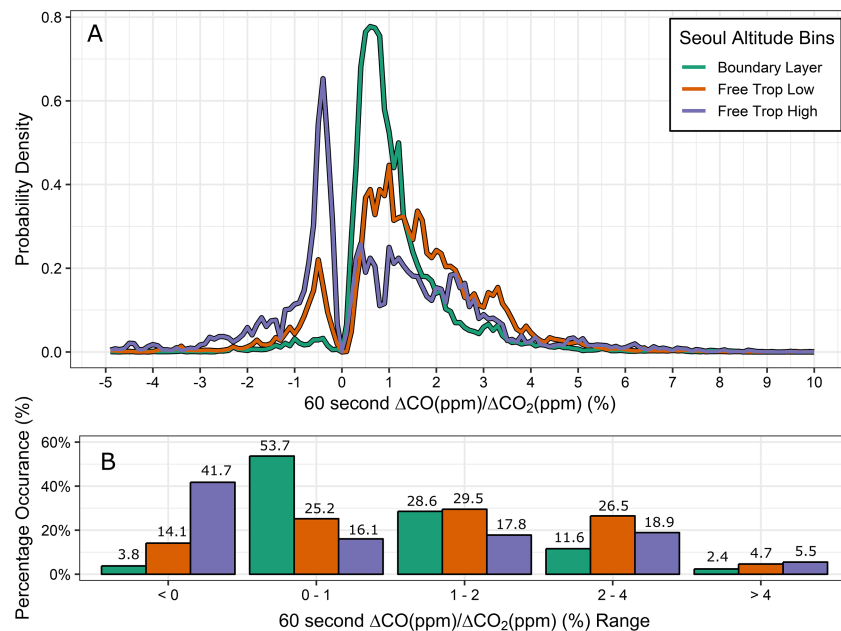


Figure 6. Vertically binned distributions in the Seoul analysis region. (a) The slope distributions for observations collected over Seoul, colored by vertical bin: the boundary layer, the low free troposphere (alt < 3 km ASL, pressure altitude), and the high free troposphere (alt ≥ 3 km ASL). (b) Quantification of the distributions by $\Delta\text{CO}/\Delta\text{CO}_2$ ratio range. Each bar is colored by vertical bin and labeled with the percentage of the distribution that occurs within the listed range. ASL = above sea level.

ASL). The distributions of the correlated slopes are quantified by ratio range in Figure 6b. In the boundary layer the distribution of ratios is narrow, centered on 0.5% $\Delta\text{CO}/\Delta\text{CO}_2$, with the majority of the correlated slopes (>80%) occurring between 0% and 2% $\Delta\text{CO}/\Delta\text{CO}_2$. Moving higher in the atmosphere, two trends occur. First, above the boundary layer the distributions show a larger contribution from higher ratios, showing a shift to lower-efficiency-type distribution. Second, the proportion of negative slopes also increases with increasing altitude, indicating that the biogenic signature in $\Delta\text{CO}/\Delta\text{CO}_2$ becomes more important with altitude. In the high free troposphere, approximately 42% of the correlated slopes are negative.

The cumulative distribution functions (CDFs) for the vertically split correlated slope distributions are shown in Figure 7. CDFs show how much of the distribution is below a specific value—for instance, for this work the value at zero indicates what percentage of the distribution has a negative correlated slope. This facilitates comparison of the distributions without needing to account for exactly where local peaks in the distribution occur. Figure 7a shows the CDFs for the full range slope values, while Figure 7b shows the CDFs for the positive slopes only and Figure 7c shows the CDFs for the negative slopes only. The full range CDFs in Figure 7a show that negative slopes have a greater contribution to the slope distributions at high altitudes and that there is also a shift in the positive slopes to higher $\Delta\text{CO}/\Delta\text{CO}_2$ ratios, as seen in Figure 6. The positive slope CDFs in Figure 7b show this move to higher ratios with altitude in more detail, with the boundary layer data having a clearly sharper distribution with lower $\Delta\text{CO}/\Delta\text{CO}_2$ ratios overall. In comparison, the low free tropospheric and high free tropospheric bins overlap significantly in the positive slope CDFs, with a noticeable divergence only occurring around 3.5% $\Delta\text{CO}/\Delta\text{CO}_2$, when the highest altitude bin shows an additional contribution from higher ratios. The high free troposphere bin has a CDF that is shallower than the low free tropospheric bin for all slopes greater than 1% $\Delta\text{CO}/\Delta\text{CO}_2$, but the difference is slight.

The negative slope CDFs in Figure 7c show the same divergence between the boundary layer and the two free tropospheric bins, for slightly different reasons. While the boundary layer bin has a sharper distribution with lower ratio slopes compared to the free troposphere, in the negative slopes the boundary layer CDF indicates that the distributions of the negative slopes in that lowest level of the atmosphere are shifted to more negative values, while both of the free tropospheric bins produce negative slopes at roughly the same $\Delta\text{CO}/\Delta\text{CO}_2$ ratios. Taken together, these results indicate that over the Seoul analysis region the $\Delta\text{CO}/\Delta\text{CO}_2$ slope

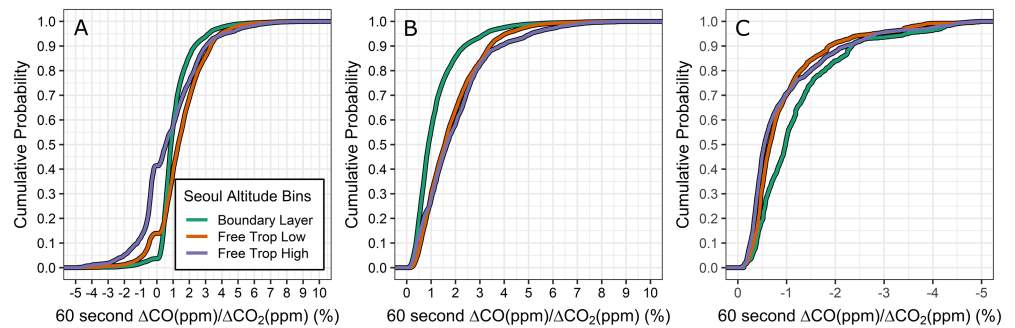


Figure 7. Seoul slope distribution cumulative distribution function plots (CDFs). The lines are colored by vertical bin. (a) The CDFs for the full slope distribution range. (b) The CDFs for the positive slopes only. (c) The CDFs for the negative slopes only; note that the x axis is reversed for clearer comparison to the other panels. Removing the negative slopes from the CDFs allows comparison of the slope distributions between the three vertical bins over Seoul without needing to account for the large proportion of negative slopes that are measured above 3 km ASL (the high free troposphere); removing the positive slopes allows for comparison of the where each height bin picks up the largest proportion of negative slopes.

distributions have different behavior above and below the boundary layer, with that boundary layer/free tropospheric difference captured in both the positive and negative slopes. Once in the free troposphere, the main differences between the high and low free tropospheric bins is the proportion of negatively correlated $\Delta\text{CO}/\Delta\text{CO}_2$ slopes, and the distributions pick up an additional slight enhancement in the high-ratio slopes with higher altitude in the free troposphere.

Interpreting the negative slopes as the primary indicator of biogenic activity returns the perhaps unexpected result of indicating larger losses of CO_2 to biogenic uptake at higher altitudes. However, Turnbull, Tans, et al. (2011) observed that far-field measurements of CO_2 on the west coast of South Korea were dominated by terrestrial sources, with only 20% of their far-field (not South Korean originating) CO_2 being attributable to fossil fuel sources. The low free tropospheric and high free tropospheric measurements over Seoul are associated with higher wind speeds, and in general higher-altitude measurements favor long-distance transport compared to boundary layer measurements, which are influenced by local sources. Turnbull et al. attributed a larger fraction of their measurements to biogenics compared to this work, which is only attributing periods of negative slopes to biogenic behavior; however, Turnbull et al. included combustion processes like biomass burning in the terrestrial sources, while this technique would identify that kind of process with a positive $\Delta\text{CO}/\Delta\text{CO}_2$ slope.

3.3. The West Sea Receptor Location Analysis

3.3.1. Overall West Sea Receptor Analysis

The West Sea analysis region can be treated as a receptor location, useful for looking at the advection inflow to the Korean Peninsula over water where there are few significant direct emissions. Since there were many flights that included legs in this analysis region over different meteorological regimes, it is helpful to split the flights in this analysis region into three subdivisions, shown in Figure 1. Figure 8 shows the $\Delta\text{CO}/\Delta\text{CO}_2$ slope distributions (Figure 8a), slope quantification by ratio range (Figure 8b), and back trajectory wind crosses (Figures 8c–8e) for these three West Sea analysis sectors.

Sector A is the South Korean outflow region, which shows extremely low ratio positive $\Delta\text{CO}/\Delta\text{CO}_2$ slopes, few negative slopes, and wind crosses centered over the Korean Peninsula, but covering a wide expanse both east and west due to the wind direction moving from a primarily easterly flow to a primarily westerly flow with altitude. Sector B shows a change in the $\Delta\text{CO}/\Delta\text{CO}_2$ distributions to higher ratios compared to Sector A, with the wind cross centers moving to the west; this sector is considered mixed South Korean inflow and outflow. Sector C encompasses the measurements that were made on the far western side of the West Sea analysis region, which targeted Chinese inflow to South Korea, and the $\Delta\text{CO}/\Delta\text{CO}_2$ distributions show a flat, wide distribution dominated by high ratios and indicating low-efficiency combustion type slopes relative to the other two West Sea analysis region sectors. The Sector C wind cross is also centered westward from both Sectors A and B, indicating that Sector C is a Chinese source/Korean inflow measurement.

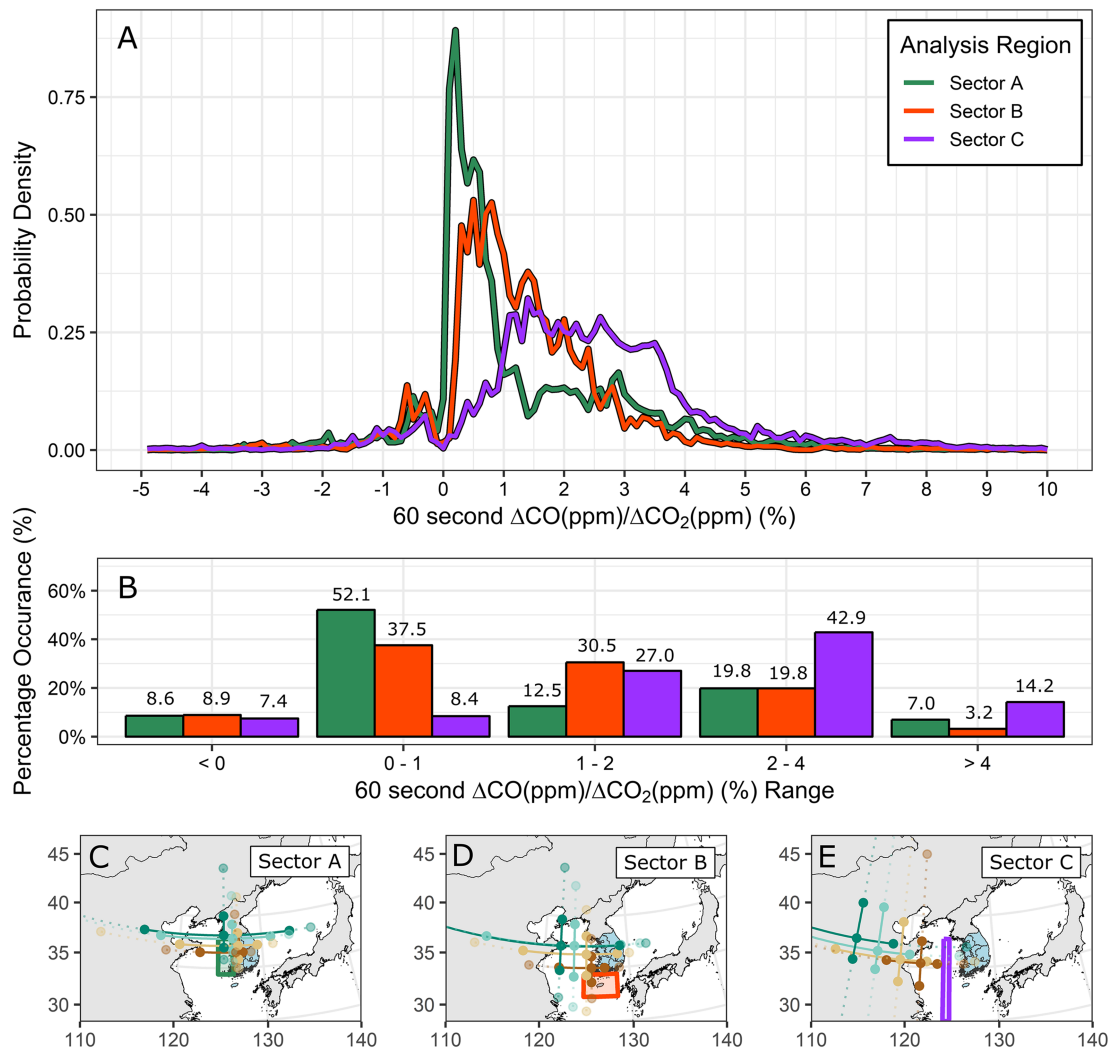


Figure 8. Slope distributions for the West Sea analysis sectors (Figure 1). (a) Slope distributions for the three analysis sectors, colored by sector. (b) Quantification of the distributions by $\Delta\text{CO}/\Delta\text{CO}_2$ ratio range. Each bar is colored by sector and labeled with the percentage of the distribution that occurs within the listed range. (c–e) The back trajectory wind crosses for the three West Sea sectors, colored by back trajectory hour as in Figure 2. Each map has a polygon of the sector footprint, colored by sector.

While Sector A has an extremely sharp distribution indicative of primarily low ratio emissions (>50% of the correlated slopes between 0% and 1% $\Delta\text{CO}/\Delta\text{CO}_2$), Sector B shows a shift in these distributions with nearly 70% of the correlated slopes falling between 0% and 2% $\Delta\text{CO}/\Delta\text{CO}_2$, but only 37.5% of them occurring between 0% and 1% $\Delta\text{CO}/\Delta\text{CO}_2$. In contrast, Sector C shows a very distinct change in the distributions, with a higher percentage of high ratios and few correlated slopes falling in the highest-efficiency region, 0–1% $\Delta\text{CO}/\Delta\text{CO}_2$. Most of the Sector C slopes (69.6%) fall between 1% and 4% $\Delta\text{CO}/\Delta\text{CO}_2$.

3.3.2. Vertical West Sea Receptor Analysis

The West Sea sector analysis indicates that the distribution moving to a higher ratio (lower efficiency) is associated with air masses originating over China. While this makes intuitive sense, as the efficiency of the combustion sources in China are expected to be lower overall compared to sources in South Korea (Silva et al., 2013), the sector results need to be examined in more detail.

Figure 9 shows the $\Delta\text{CO}/\Delta\text{CO}_2$ slope distributions for the three West Sea analysis sectors split by vertical bin. Figures 9d–9f quantify the slope distributions by ratio range. The plots are organized vertically, from high- to low-altitude bin. When split this way, the distribution differences between the three West Sea analysis region sectors show clear differences by vertical split and analysis sector. Figure 10 shows the back trajectory wind

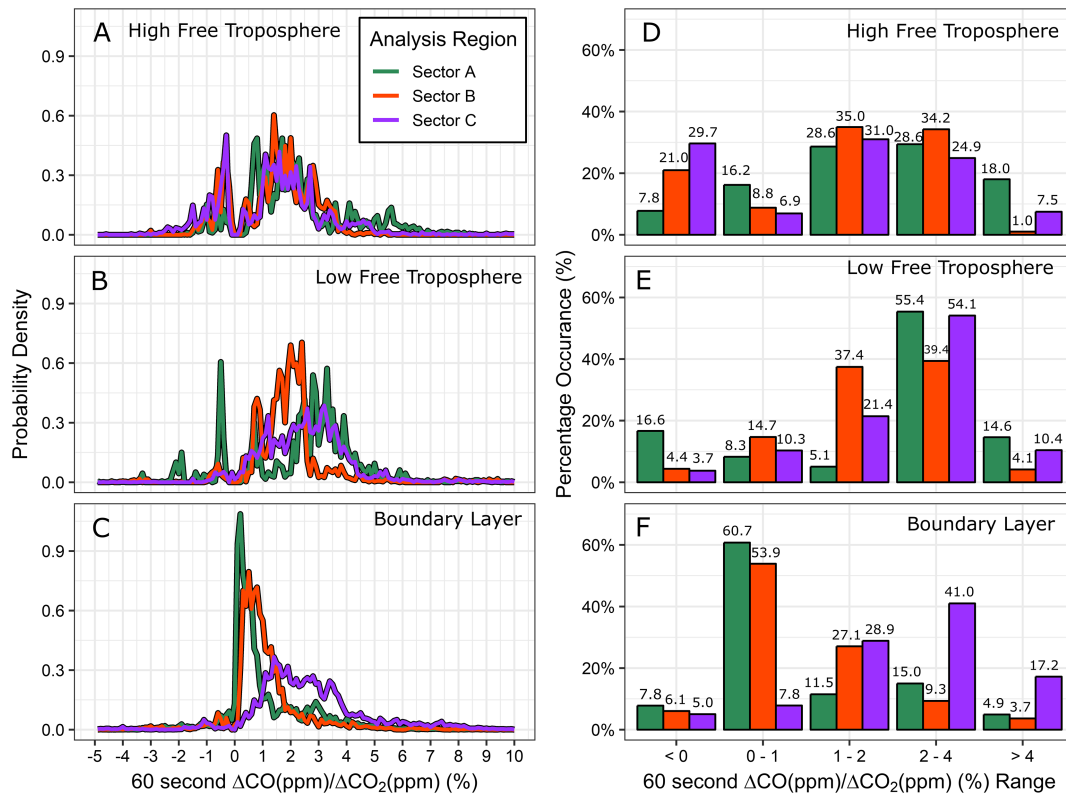


Figure 9. West Sea analysis sectors, separated by vertical bin. (a–c) The slope distributions colored by analysis sector and organized by vertical bin, high to low. (d–f) Quantification of the slope distributions, organized by ratio range and colored by analysis sector and labeled with the percentage of the distribution that occurs within the listed range. (a, d) The high free troposphere, (b, e) low free troposphere, and (c, f) boundary layer data.

crosses by West Sea sector and altitude bin. Quantification of the relative sampling level for all regions is recorded in the supporting information.

In the high free troposphere (Figures 9a and 9d) all three sectors show similar $\Delta\text{CO}/\Delta\text{CO}_2$ slope distributions, with back trajectories (Figure 10, high free troposphere) that show consistent behavior between the three sectors. All three regions are associated with fast westerly winds and show slope distributions that have positive slopes that are shifted to higher ratios with the bulk of the correlated slopes between 1% and 4% $\Delta\text{CO}/\Delta\text{CO}_2$, with the distributions from all three altitude bins showing very similar behavior. All three regions also have significant negative slopes in this highest altitude bin.

Moving downward, the low free tropospheric data (Figures 9b and 9e) begin to show divergence in both the $\Delta\text{CO}/\Delta\text{CO}_2$ slope distributions and the back trajectory wind crosses (Figure 10, low free troposphere) between sectors. However, while the three sectors have differences between the exact placement of the distribution shape and peak, all three are still clearly dominated by high-ratio slopes, with approximately 90% of the slopes for all three sectors falling between 2% and 4% $\Delta\text{CO}/\Delta\text{CO}_2$. Additionally, the positive slope distributions for Sectors A and C have similar shapes (Figure 9b), while the back trajectories for these two regions likewise show similar spatial influence. In contrast, Sector B has a distribution that peaks at approximately 2% $\Delta\text{CO}/\Delta\text{CO}_2$ and back trajectories that also originate in China, but with a significantly more southerly component compared to Sectors A and C.

The West Sea analysis sector differences are most distinct in the boundary layer. The boundary layer $\Delta\text{CO}/\Delta\text{CO}_2$ slope distributions (Figures 9c and 9f) show significant differences between sectors and have notable differences in the sector wind crosses (Figure 10, boundary layer). All three regions have small contributions from negative slopes (<10% of the total correlated slopes), but there are large differences in the positive slopes. Sectors A and B both have more than 50% of their slopes in the lowest ratio range of 0–1% $\Delta\text{CO}/\Delta\text{CO}_2$. The slope distributions are also very narrow for these two sectors, centered at 0.1% $\Delta\text{CO}/\Delta\text{CO}_2$ for

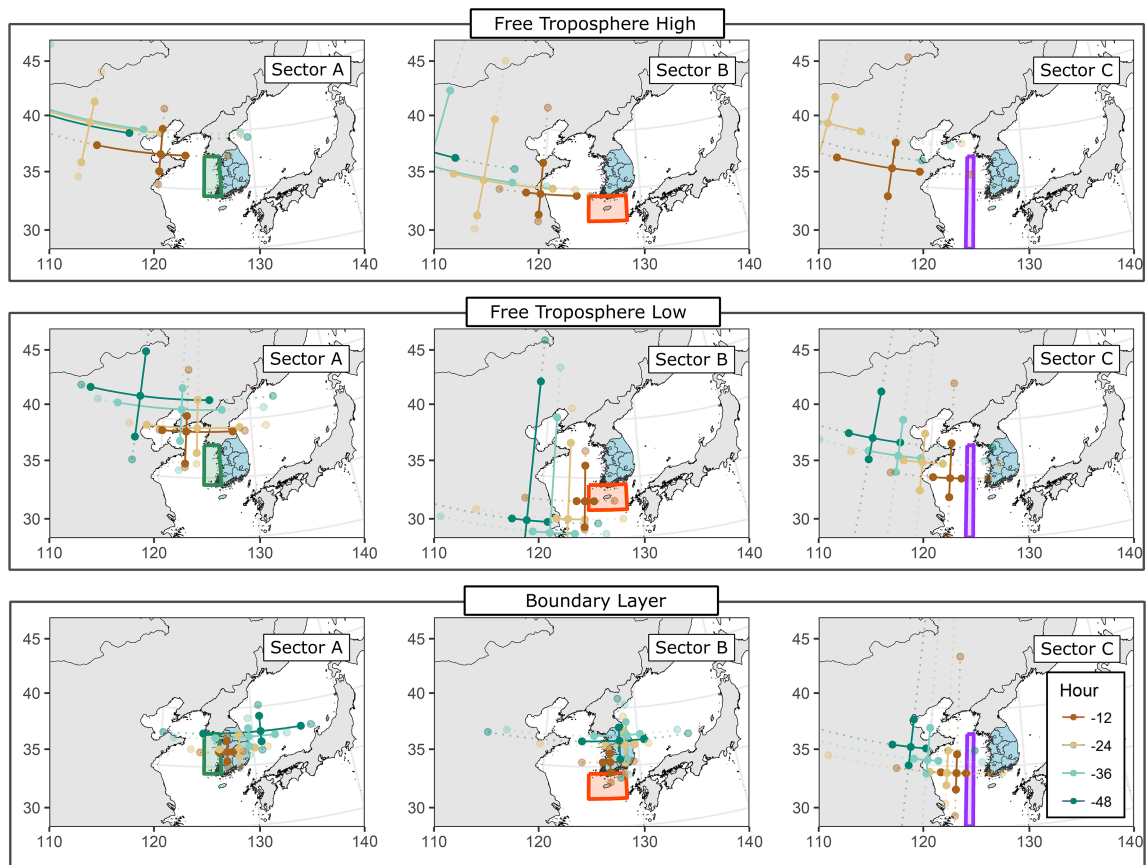


Figure 10. Wind crosses for the West Sea analysis sectors by altitude bin. The wind crosses are colored by back trajectory hour. Each map has a polygon of the appropriate sector footprint, colored by sector. The maps are organized by vertical bin, from high to low altitude.

Sector A and 0.5% $\Delta\text{CO}/\Delta\text{CO}_2$ for Sector B. Additionally, both Sectors A and B have wind crosses that very clearly originate over the Korean Peninsula within 48 hr of measurement and stay over or to the east of the peninsula for a full 48 hr prior to the sampling. This indicates that the slope distributions measured for Sectors A and B in the lowest-altitude bins can be considered indicative of ratios expected for the mixed emission from the Korean Peninsula. These results also match the lowest altitude slope distributions over the Seoul analysis region.

A note on Sector A: These measurements are not only a receptor location for the emissions from the Korean Peninsula but also encompasses power plant emissions from the industrial sector on the West coast of Korea. Power plant combustion efficiencies are typically very high, with very small amounts of CO produced compared to CO₂ emissions, leading to the result over Sector A in the lowest-altitude bin where the slope distribution peaked at 0.1% $\Delta\text{CO}/\Delta\text{CO}_2$. The results from this boundary layer sector should be considered indicative of the power plant generation on the west coast of South Korea, rather than a characterization of the general South Korean combustion signature; in contrast, the Sector B boundary layer data is more indicative of the general South Korean outflow signature.

Finally, boundary layer slope distributions for Sector C are clearly characteristic of higher $\Delta\text{CO}/\Delta\text{CO}_2$ ratios compared to Sectors A and B and indicate sources with lower-efficiency combustion. Fewer than 10% of the correlated slopes for Sector C are in the highest efficiency bin, 0–1% $\Delta\text{CO}/\Delta\text{CO}_2$, while roughly 70% of the slopes fall between 1% and 4% $\Delta\text{CO}/\Delta\text{CO}_2$, with more than half of those high-ratio slopes occurring between 2% and 4% $\Delta\text{CO}/\Delta\text{CO}_2$. The wind cross for Sector C (Figure 11, boundary layer) also indicates that the air masses measured in this analysis sector originate to the west of the region. The West Sea Sector C results can be considered a Chinese-sourced high-ratio distribution, arising from low-efficiency combustion compared to the South Korean originated air masses.

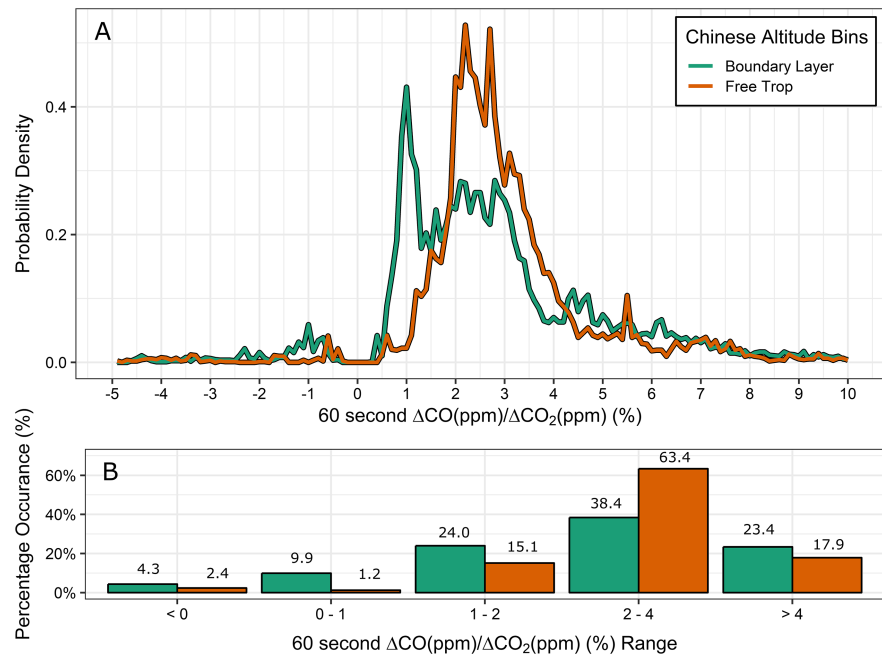


Figure 11. Vertically binned distributions of the Chinese data. (a) The slope distributions for observations collected over China, colored by vertical bin: the boundary layer and the free troposphere. (b) Quantification of the distributions by $\Delta\text{CO}/\Delta\text{CO}_2$ ratio range. Each bar is colored by vertical bin and labeled with the percentage of the distribution that occurs within the listed range.

The vertical breakout of the West Sea analysis sectors (Figures 9 and 10) shows that the differences in the overall West Sea sector distributions (Figure 9) can be attributed to differences in the air masses measured in the boundary layer. The free tropospheric measurements over the three West Sea analysis sectors were associated with fast moving westerly winds, and all three sectors also showed a change in $\Delta\text{CO}/\Delta\text{CO}_2$ slope distributions to higher ratios, in both the low and high free troposphere with greater distribution agreement in the high free troposphere. However, in the boundary layer the distributions for the three sectors differ, with an accompanying change in the associated back trajectories. The boundary layer measurements were more heavily influenced by local and short-range sources, due to the lack of time to dilute sources into the free troposphere, and these boundary slope distributions are considered to be indicative of the source signature for South Korea (Sector B) and China (Sector C).

3.4. Chinese Aircraft Measurements

Based on the results from the West Sea sector analysis, there is a strong source signature in the slope distributions, with air masses advecting from China having $\Delta\text{CO}/\Delta\text{CO}_2$ slope distributions that have a larger contribution from high-ratio measurements, indicating the influence of lower-efficiency combustion. To confirm these results, we use the measurements collected over China on a Chinese in situ measurement aircraft during the KORUS-AQ sampling period. The flight paths from the Chinese data set are shown in Figure 1, and the slope distributions from these data are presented in Figure 11, separated by altitude bin. Figure 11b quantifies these vertically split slope distributions.

The Chinese data set is split vertically into a boundary layer and a free troposphere layer; the altitude range of the smaller aircraft used during these measurements was smaller than the KORUS-AQ South Korean measurements made from the NASA DC-8, and the maximum altitude reached in the Chinese data set was 3.6 km ASL, so a high free troposphere bin (≥ 3 km ASL) was not included. The vertical splits over Seoul and the West Sea analysis regions generally showed a shift to higher ratios and wider distributions with increasing height; in the Chinese data, the free tropospheric measurements are shifted to a higher ratio compared to the boundary layer measurements, but the distribution at altitude is narrower, with 64% of the correlated slopes occurring between 2% and 4% $\Delta\text{CO}/\Delta\text{CO}_2$. The free tropospheric slope distribution peaks between

2% and 3% $\Delta\text{CO}/\Delta\text{CO}_2$, while the boundary layer slopes have a bimodal distribution, peaking at 1% and approximately 2.5% $\Delta\text{CO}/\Delta\text{CO}_2$. The boundary layer slopes also show a greater spread in the distributions, with a larger number of correlated slopes below 2% $\Delta\text{CO}/\Delta\text{CO}_2$ and above 4% $\Delta\text{CO}/\Delta\text{CO}_2$ compared to the free troposphere, indicating that there is a wider mix of sources close to the surface compared to the free troposphere.

However, even with the difference between the boundary layer and free tropospheric $\Delta\text{CO}/\Delta\text{CO}_2$ slopes in the Chinese data, there is a clear shift to higher ratios in these slope distributions compared to the $\Delta\text{CO}/\Delta\text{CO}_2$ ratios measured on the Korean Peninsula. The total slope distributions in the Chinese data show that only 6% of the correlated slopes fall between 0% and 1% $\Delta\text{CO}/\Delta\text{CO}_2$, and roughly half of the correlated slopes measured over China are between 2% and 4% $\Delta\text{CO}/\Delta\text{CO}_2$. There are more slopes with a ratio $>4\%$ $\Delta\text{CO}/\Delta\text{CO}_2$ range than there are high-efficiency type slopes (0–1% $\Delta\text{CO}/\Delta\text{CO}_2$) or negative slopes.

The Chinese data set was collected downwind from the Gobi Desert, over a mixed-use industrial, agricultural and suburban region. The wide mix of sources at the surface in the boundary layer is expected based on the use characteristics of the region, as is the change in the overall slope distributions to a lower-efficiency type compared to the results over South Korea. An additional difference between these measurements and the South Korean measurements is how the slope distributions narrow in the free troposphere; where the free tropospheric measurements over South Korea show the slope distributions becoming both broader and more negative when compared to the boundary layer, the free tropospheric measurements over China show a distribution that is sharper and with lower ratios compared to the boundary layer. There are also very few negative slopes measured in the Chinese dataset. The lower-efficiency peak in the Chinese distributions for both the boundary layer and the free troposphere peak at approximately 2.5% $\Delta\text{CO}/\Delta\text{CO}_2$, possibly indicating some common source type between the two altitudes. The peak at 1% $\Delta\text{CO}/\Delta\text{CO}_2$ in the boundary layer indicates that there is some source in the study region that is running at relatively high efficiency; this could be attributed to vehicles or power generation, without similar sources upwind of the sampled region.

3.5. Seoul Versus China Versus West Sea Subregion C

The slope distribution for the overall Seoul analysis region is dominated by low-ratio slopes (Figure 4), indicating overall higher-efficiency emissions from the region into the boundary layer; However, the vertically separated Seoul analysis region (Figure 6) indicated that the correlated slopes shifted to higher distributions at high altitudes, suggesting that a Chinese emissions signature may be influencing the $\Delta\text{CO}/\Delta\text{CO}_2$ slopes in the free troposphere over Seoul. To better understand this behavior, Figure 12 compares the vertically separated distributions from the Seoul analysis region to the full-altitude distributions observed in China and over the West Sea Sector C boundary layer (Chinese-sourced inflow to South Korea), and to the South Korea outflow into the West Sea Sector B boundary layer (section 4.3). Figures 12a–12c show the $\Delta\text{CO}/\Delta\text{CO}_2$ slope distribution comparisons between the vertically separated Seoul data and the three full-altitude comparison distributions, where all three comparison distributions are identical in the three subplots. The slope distributions are quantified by ratio range in Figures 12d–12g. Figure 13 shows the CDF plots for these comparisons, with the full range distributions (Figures 13a–13c) and the positive-slope-only distributions (Figures 13d–13f).

The Seoul boundary layer distribution (Figure 12c) compares extremely well to the West Sea Sector B boundary layer measurements, which we consider to be the South Korean Peninsula outflow $\Delta\text{CO}/\Delta\text{CO}_2$ signature. There are minor contributions from negative slopes (roughly 5% or less), and both distributions have more than 50% of their correlated slopes between 0% and 1% $\Delta\text{CO}/\Delta\text{CO}_2$ and 80% of the correlated slopes below 2% $\Delta\text{CO}/\Delta\text{CO}_2$ (Figures 12f and 12g). The positive slope CDFs (Figure 13) also show that the Seoul boundary layer the West Sea region B slope distributions have very similar distributions. In contrast, the two Chinese distributions, the Chinese data and the West Sea Sector C boundary layer, show distributions that are similarly very well matched to each other, but with higher ratios compared to the South Korean-type distributions (Seoul boundary layer and West Sea Sector B boundary layer; Figures 13c and 3f).

Our previous analysis of the Seoul vertical distributions (section 4.2) indicated that there was a clear distribution change in the positive slopes over the Seoul analysis region, with the free tropospheric data showing a distinct $\Delta\text{CO}/\Delta\text{CO}_2$ distribution signature from the Seoul analysis region boundary layer data, (Figure 7b).

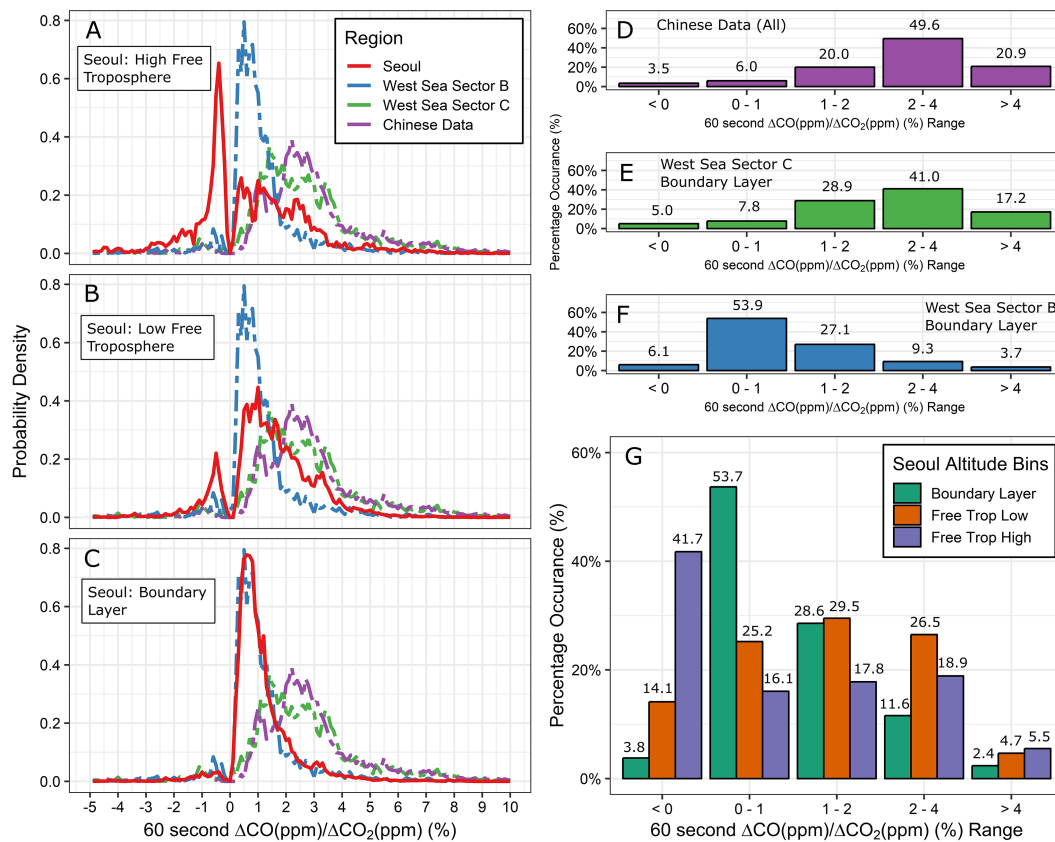


Figure 12. Comparison between the Seoul, the West Sea Region B Boundary Layer, the West Sea Region C Boundary Layer, and the Chinese data, split by the vertical bins of the Seoul analysis region. (a–c) The slope distributions for the three regions, colored by region. The distribution is a normalized probability density plot for direct comparison of the distributions. In all three panels the West Sea Region B Boundary Layer distributions, West Sea Region C Boundary Layer Distributions, and Chinese distribution are the same distributions, not split by altitude. The Seoul slope distribution is split by altitude bin, as noted on the panel. (d) Quantification of the Chinese dataset slope distributions by $\Delta\text{CO}/\Delta\text{CO}_2$ ratio range. All altitude data are included. (e) Quantification of the West Sea Sector C boundary layer slope distribution by $\Delta\text{CO}/\Delta\text{CO}_2$ ratio range. This is the Chinese-sourced Korean inflow signature. (f) Quantification of the West Sea Sector B boundary layer slope distribution by $\Delta\text{CO}/\Delta\text{CO}_2$ ratio range. This is the South Korea outflow signature. (g) Quantification of the Seoul analysis region slope distributions by $\Delta\text{CO}/\Delta\text{CO}_2$ ratio range, grouped and colored by Seoul vertical bin.

Figures 13b and 13e show the slope distributions of the low free tropospheric Seoul analysis region data compared to the same South Korean outflow signature, the Chinese-sourced inflow signature, and the direct Chinese emissions; Figures 13a and 13d show high free tropospheric Seoul $\Delta\text{CO}/\Delta\text{CO}_2$ distributions against the same data. The full range CDFs (Figures 13a and 13b) are included for completeness and show the increased proportion of negative slopes in the high altitude Seoul data; however, the positive slope CDFs (Figures 13d and 13e) show the more important comparison. When the negative slopes are disregarded, the Seoul high free tropospheric (Figure 13d) and Seoul low free tropospheric (Figure 13e) distributions fall between the South Korean outflow signature (West Sea Sector B boundary layer) and the Chinese signature (Chinese measurements and West Sea Sector C boundary layer). While the Seoul $\Delta\text{CO}/\Delta\text{CO}_2$ distributions show a slight shift to higher ratios in the high free troposphere compared to the low free troposphere (Figure 12g), this change is very slight and does not turn the Seoul positive slope distribution in the highest altitude bin into a fully Chinese type distribution.

There are three conclusions from this comparison. First, the West Sea Sector C boundary layer and Chinese data have very similar ratio signatures. While the measurements in these two regions have some differences in the exact placement of the peaks, the two regions have roughly equivalent distributions, with the bulk of the correlated emissions falling between 1% and 5% $\Delta\text{CO}/\Delta\text{CO}_2$. Second, these two Chinese type distributions are shifted toward higher ratios compared to the data collected over Seoul and the South Korean outflow (West Sea Sector B boundary layer). The Seoul and South Korean outflow distributions compare

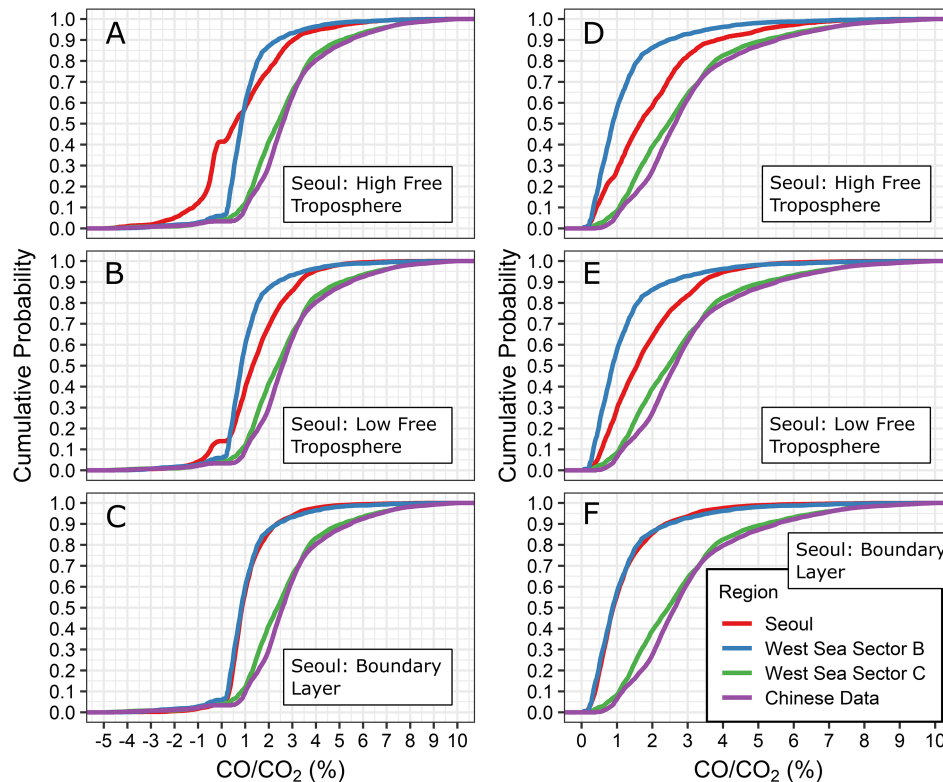


Figure 13. Cumulative distribution function (CDF) plots of the comparison between the Seoul, the West Sea Sector B Boundary Layer, the West Sea Sector C Boundary Layer data, and the Chinese data split by the vertical bins of the Seoul analysis region. The Seoul distribution changes with altitude bin; the West Sea Sector B boundary layer, the West Sea Sector C boundary layer, and Chinese CDFs are the same in each panel. (a–c) The CDFs for the full slope distribution range. (d–f) The CDFs for the positive slopes only. (a, d) The high free tropospheric Seoul slope distributions, (b, e) the low free tropospheric Seoul slope distributions, and (c, f) the boundary layer Seoul slope distributions.

extremely well, with narrow distributions that fall primarily between 0% and 2% $\Delta\text{CO}/\Delta\text{CO}_2$. This indicates a much different set of emissions between South Korea and China, with the South Korean emissions showing a low-ratio-type signature, implying higher-efficiency combustion processes, compared to the measurements associated with China. Finally, while there is a ratio shift over South Korea with altitude to higher $\Delta\text{CO}/\Delta\text{CO}_2$ ratios with increasing altitude, the Seoul measurements indicate that there is not an unambiguous Chinese outflow signature at high altitudes. A high proportion of negative slopes in the high free troposphere over Seoul indicate that the high altitude data is disproportionately impacted by a biogenic signature, the source of which is unclear in this analysis.

4. Discussion

4.1. Comparisons to Korean Emission Inventories

The slope distribution analysis provides information about what ratios of $\Delta\text{CO}/\Delta\text{CO}_2$ are most common in an analysis region, while traditional ratio calculations over longer time periods calculate the overall ratio for the blend of sources and sinks in a study region. The two pieces of information are complementary, but the ratio distributions provide detail on the range of ratios observed in the atmosphere and the relative importance of different ratio ranges, which can be used in comparisons with the emissions inventories. Table 2 shows the emissions inventory values for East Asia in 2015, from the South Korean National Institute of Environmental Research's KORUS Emissions Inventory Version 2.0, a modified version of the CREATE Inventory (Woo et al., 2013). Table 2 includes data for South Korea, North Korea, China and Japan, and for the South Korean Seoul metropolitan region. In South Korea and Japan, CO is primarily sourced from transportation, while China produces most of its CO in industry. The primary CO₂ sources for these three countries is either power generation or cooking. The primary CO₂ source for South Korea, China, and

Table 2
Emissions Inventory Values for East Asia in 2015

Emission Sector	South Korea		South Korea: Seoul only		North Korea		China		Japan	
	CO	CO ₂	CO	CO ₂	CO	CO ₂	CO	CO ₂	CO	CO ₂
Power	89.9	268.3	1.0	1.2	1.0	4.7	656.5	5,016	149.1	540.2
Industry	134.6	227.8	0.2	0.4	65.3	14.8	101,175	4112	977.1	211.4
Residential	186.6	57.7	8.8	8.1	310.7	3.7	46,296	618.4	151.0	144.8
Transportation	481.6	96.4	76.7	7.7	91.0	1.2	17,479	864.3	3,000.6	210.9
Total	941.0	648.5	86.7	17.4	534.1	24.6	165,606	10,611	4,277.8	1107

Note. CO emissions are reported in gigagrams per year. CO₂ emissions are reported in teragrams per year.

Japan is power generation. North Korea's primary CO source is residential, due to heating and cooking, while the primary CO₂ source is industry.

Table 3 shows the calculated CO/CO₂ mole ratio for each region and source calculated from the emissions in Table 2 (see supporting information section S6). The CO/CO₂ ratios are presented as percentage ratios. Using the expected emissions inventory ratio for each area (country or city), there is reasonable agreement between the expected CO/CO₂ mole ratios from the emissions inventories to the observed slope distributions. While the overall expected CO/CO₂ mole ratio for South Korea of 0.228% CO/CO₂ does not match the plotted slope distributions, the expected ratio for Seoul matches the peak in the slope distribution over the Seoul analysis region quite well, with an expected inventory ratio of 0.78.

In the inventories, transportation is the most significant CO source in Seoul, and the expected transportation ratio is 1.5% CO/CO₂; however, the observed boundary layer ratio peak over Seoul has better agreement to the overall South Korea transportation ratio of 0.80% CO/CO₂. Finally, the emissions inventories estimate that the primary CO₂ source for South Korea is power generation, followed closely by industry. The West Sea Sector A analysis in section 3.3.1 showed the results for measurements over a region with a large number of power plants and includes data from a flight with deliberate sampling of power plant emissions (21 May 2016); this Sector A analysis has a boundary layer slope distribution that had a peak below 0.5% ΔCO/ΔCO₂, indicating that the measurements were sampling the high-efficiency combustion signature expected for the area.

In contrast, the emissions inventories for China estimate an overall CO/CO₂ ratio of 2.5% CO/CO₂, which captures the change in the slope distributions to higher ratios observed in the data from both the Chinese mainland and the West Sea Sector C, in which Chinese inflow to South Korea was sampled. The emissions inventory for China indicates that both the transportation and industrial sectors have an expected overall ratio of 3% to 4% CO/CO₂, with the industrial sector dominating Chinese CO emissions, and industrial emissions a close second only to power generation in CO₂ emissions. However, the emissions ratios expected from the inventory are higher than what we see in the ΔCO/ΔCO₂ ratio distributions, with power generation the only category with an expected ratio below 1% CO/CO₂, and the residential emissions above 11% CO/CO₂. Recent work on pollution trends in East Asia by Zheng et al. (2018) indicate that CO emissions have

Table 3
East Asian Emission Ratios for CO/CO₂, Reported as Percentage CO/CO₂

Emission Sector	South Korea	South Korea: Seoul only	North Korea	China	Japan
	% CO (mole)/CO ₂ (mole)				
Power	0.053	0.126	0.033	0.021	0.043
Industry	0.093	0.090	0.692	3.866	0.726
Residential	0.508	0.171	13.04	11.76	0.164
Transportation	0.800	1.558	11.45	3.178	2.236
Total	0.228	0.784	3.416	2.453	0.607

Note. These ratios are derived from the inventory information presented in Table 2.

decreased in China while fossil fuel consumption has held steady or increased and attribute this decrease in CO to increasing emission controls within China. Assessing the change in Chinese emissions is beyond the scope of the current work, but motivates the use of this technique as a method for assessing inventory comparisons to top-down measurements, especially in areas like China where there are rapidly changing emissions characteristics.

4.2. Discussion of Method Applications

The distributions of the short-term CO to CO₂ slopes are a different way of understanding source ratios for a region; rather than calculating the overall ratio for the total mix of combustion sources, the slope distributions indicate which ratios are most common in a region. This method adds value to other types of ratio calculations, especially when there are high time resolution in situ measurements, such as the CO and CO₂ collected during KORUS-AQ.

There are some caveats to this method. First, this technique takes advantage of the fact that these two species are frequently coemitted from the same sources under the same conditions, with distinct ratios. Both of these species are also relatively long lived in the atmosphere. This technique will be more difficult with species that have short atmospheric lifetimes, or emissions ratios that are not as clearly defined. This technique also uses a correlation filtering of the calculated $\Delta\text{CO}/\Delta\text{CO}_2$ slopes and does not consider slopes with a coefficient of determination less than 0.5; this means that slopes will not be considered for time windows during which the two species are not covarying. This technique is only sensitive to regions where the concentrations are changing on short time scales, such as when the instrument samples a time varying mixture of two air masses.

Additionally, a complication of this method with these particular tracers is the use of the negative slopes to identify biogenic signatures. As we noted in the results, the attribution of biogenic signatures only to negative results returns a result that indicates that there is higher biogenic influence at high altitudes. However, the assignment of biogenic behavior only to negative slopes is overly simplistic, as biogenic CO₂ depletion of an air mass with enhanced CO₂ over the background may still have a positive slope. The lack of negative slopes at low altitudes does not indicate that there is necessarily less biogenic activity compared to high altitudes. Disentangling that dynamic is beyond the scope of the current work; however, the use of the coefficient of determination as a filter for the $\Delta\text{CO}/\Delta\text{CO}_2$ allows us to have some confidence that this method is able to characterize nearfield emissions and coherent plumes.

Despite these limitations, the technique is able to provide information about correlated species over a region or period of time and provide a CO/CO₂ ratio signature, which can be used to understand trends or differences in combustion sources between regions. This analysis shows that the technique can be used to characterize a source signature distribution, and how these ratio distributions can be used in areas with heterogeneous source characteristics (e.g., China vs. South Korea) to differentiate between air mass origins. Combining these kinds of ratio calculations with additional chemical species and with modeled source tracers present exciting analysis opportunities in the KORUS-AQ data set and beyond.

This method of ratio characterization is not intended to replace general ratios between two species, but to supplement that analysis. The short-term ratio analysis will be useful in scenarios where high time resolution data sets of chemical species are available; aircraft and tower studies are particularly well suited to leverage this technique for added information about air mass characteristics. Additionally, potential applications include using this method to assess sources during severe air quality events in well-measured regions, and for inventory assessment in areas with changing air quality regulations and types of sources.

5. Conclusions

Ratios of CO to CO₂ provide information about the emissions within a study region. While correlation over a region or period of time may provide information about the overall mix of sources and sinks, the distributions of the ratios collected from a rolling correlation with a short time period allows us greater insight into the short-term and near-range sources. The distributions of the calculated slopes can be loosely interpreted as a low-ratio-type distribution, with slopes primarily between 0% and 2% $\Delta\text{CO}/\Delta\text{CO}_2$, or a high-ratio-type distribution, with slopes primarily above 2% $\Delta\text{CO}/\Delta\text{CO}_2$.

This technique was used on the 2016 KORUS-AQ field campaign data to investigate emissions of CO₂ and CO over the Korean Peninsula. The data set was divided into three analysis regions: the Seoul metropolitan region, which was primarily urban; the South Korean Peninsula region, which encompassed the mixed-use environment outside of Seoul over South Korea and some measurements over Japan; and the West Sea analysis region, which was treated as a receptor location for inflow/outflow over the Korean Peninsula. The Seoul analysis region showed high-efficiency type slope distributions in the boundary layer, with most of the correlated slopes between 0% and 2% $\Delta\text{CO}/\Delta\text{CO}_2$, and slope distributions that show a larger contribution from higher ratios with altitude, indicating that there was a difference in the air mass sources that was related to altitude over the Seoul analysis region. A larger proportion of negative slopes was also measured at high altitude over the Seoul analysis region than lower in the atmosphere over the same region, indicating that the biogenic signature varies with altitude in this region.

To better understand this change in slope distributions with altitude over Seoul, the West Sea analysis region was divided into three analysis sectors, which targeted different meteorological regimes: Sector A, the west coast and outflow from Seoul; Sector B, the mixed inflow to and outflow from South Korea; and Sector C, primarily Chinese sourced inflow into Korea. Analyzing these three sectors by altitude bin provided evidence that the Korean outflow shows a distinctly narrow slope distribution centered at 0.5–0.9% $\Delta\text{CO}/\Delta\text{CO}_2$, with most of the correlated slopes falling between 0% and 2% $\Delta\text{CO}/\Delta\text{CO}_2$, as seen in the Seoul boundary layer and West Sea Sectors A and B boundary layer distributions. In contrast, the Chinese-sourced inflow and direct measurements over the Chinese mainland show broadened $\Delta\text{CO}/\Delta\text{CO}_2$ distributions with generally higher ratios, with the majority of the correlated slopes falling between 1% and 4% $\Delta\text{CO}/\Delta\text{CO}_2$, and more than half of that range between 2% and 4% $\Delta\text{CO}/\Delta\text{CO}_2$. Comparing the vertical Seoul distributions to the South Korean outflow signature (West Sea Sector B boundary layer) and the Chinese-type distributions (the Chinese measurements and the West Sea Sector C boundary layer) indicated that there is a change in the distributions from a high-efficiency environment at the surface, with slopes primarily between 0% and 2% $\Delta\text{CO}/\Delta\text{CO}_2$, to a lower-efficiency environment with altitude. These measured ratio trends over South Korea are consistent with inventoried CO and CO₂ emissions, while the Chinese ratios, both measured directly and in the inflow region over the Yellow Sea, indicate a potential discrepancy between our measurements of the Chinese outflow signature and the emissions inventory.

Acknowledgments

The authors thank Jason Schroeder for the analysis region boundaries, and Jung-Hun Woo for the Korean Emissions Inventory data. Additionally, we thank Jim Crawford for campaign leadership, feedback, and guidance. Thanks to USRA, for funding the NASA Postdoc Program (NPP) Fellowship that supported this work. Additional support was provided by the Tropospheric Composition Program in the NASA Earth Science Division. Data collection was funded by the KORUS-AQ project. The field study in China was funded by the National Basic Research Program of China “973” (Grant 2013CB955801) and the National Science Foundation of the United States (Grant 1558259). The authors also appreciate the three detailed, thoughtful reviews that improved the paper. All data used in this publication are open access and can be found in the KORUS-AQ Data Archive (<https://www-air.larc.nasa.gov/missions/korus-aq/>).

References

- Andreae, M. O., & Merlet, P. (2001). Emission of trace gases and aerosols from biomass burning. *Global Biogeochemical Cycles*, *15*(4), 955–966. <https://doi.org/10.1029/2000GB001382>
- Bakwin, P. S., Tans, P. P., Zhao, C., Ussler, W., & Quesnell, E. (1995). Measurements of carbon dioxide on a very tall tower. *Tellus B*, *47*(5), 535–549. <https://doi.org/10.1034/j.1600-0889.47.issue5.2.x>
- Cantrell, C. A. (2008). Technical note: Review of methods for linear least-squares fitting of data and application to atmospheric chemistry problems. *Atmospheric Chemistry and Physics*, *8*(17), 5477–5487. <https://doi.org/10.5194/acp-8-5477-2008>
- Chan, C. K., & Yao, X. (2008). Air pollution in mega cities in China. *Atmospheric Environment*, *42*(1), 1–42. <https://doi.org/10.1016/j.atmosenv.2007.09.003>
- Chung, Y. S., & Kim, H. S. (2008). Observations of massive air-pollution transport and associated air quality in the Yellow Sea region. *Air Quality, Atmosphere & Health*, *1*(2), 69–79. <https://doi.org/10.1007/s11869-008-0014-y>
- Fang, M., Chan, C. K., & Yao, X. (2009). Managing air quality in a rapidly developing nation: China. *Atmospheric Environment*, *43*(1), 79–86. <https://doi.org/10.1016/j.atmosenv.2008.09.064>
- Ghim, Y. S., Moon, K.-C., Lee, S., & Kim, Y. P. (2005). Visibility trends in Korea during the past two decades. *Journal of the Air & Waste Management Association*, *55*(1), 73–82. <https://doi.org/10.1080/10473289.2005.10464599>
- Halliday, H. S., Thompson, A. M., Wisthaler, A., Blake, D. R., Hornbrook, R. S., Mikoviny, T., et al. (2016). Atmospheric benzene observations from oil and gas production in the Denver-Julesburg Basin in July and August 2014. *Journal of Geophysical Research: Atmospheres*, *121*, 11,055–11,074. <https://doi.org/10.1002/2016JD025327>
- Han, Y.-J., Kim, T.-S., & Kim, H. (2008). Ionic constituents and source analysis of PM_{2.5} in three Korean cities. *Atmospheric Environment*, *42*(19), 4735–4746. <https://doi.org/10.1016/j.atmosenv.2008.01.047>
- Han, S., Kondo, Y., Oshima, N., Takegawa, N., Miyazaki, Y., Hu, M., et al. (2009). Temporal variations of elemental carbon in Beijing. *Journal of Geophysical Research*, *114*, D23202. <https://doi.org/10.1029/2009JD012027>
- Hanushek, E. A., & Woessmann, L. (2016). Knowledge capital, growth, and the East Asian miracle. *Science*, *351*(6271), 344–345. <https://doi.org/10.1126/science.aad7796>
- Heald, C. L., Jacob, D. J., Fiore, A. M., Emmons, L. K., Gille, J. C., Deeter, M. N., et al. (2003). Asian outflow and trans-Pacific transport of carbon monoxide and ozone pollution: An integrated satellite, aircraft, and model perspective. *Journal of Geophysical Research*, *108* (D24), 4804. <https://doi.org/10.1029/2003JD003507>
- Heo, J.-B., Hopke, P. K., & Yi, S.-M. (2009). Source apportionment of PM_{2.5} in Seoul, Korea. *Atmospheric Chemistry and Physics*, *9*(14), 4957–4971. <https://doi.org/10.5194/acp-9-4957-2009>
- Huo, H., Zhang, Q., He, K., Yao, Z., Wang, X., Zheng, B., et al. (2011). Modeling vehicle emissions in different types of Chinese cities: Importance of vehicle fleet and local features. *Environmental Pollution*, *159*(10), 2954–2960. <https://doi.org/10.1016/j.envpol.2011.04.025>

- Kang, C.-M., Kang, B.-W., & Lee, H. S. (2006). Source identification and trends in concentrations of gaseous and fine particulate principal species in Seoul, South Korea. *Journal of the Air & Waste Management Association (1995)*, *56*(7), 911–921. <https://doi.org/10.1080/10473289.2006.10464506>
- Kang, C.-M., Sunwoo, Y., Lee, H. S., Kang, B.-W., & Lee, S.-K. (2004). Atmospheric concentrations of PM 2.5 trace elements in the Seoul urban area of South Korea. *Journal of the Air & Waste Management Association*, *54*(4), 432–439. <https://doi.org/10.1080/10473289.2004.10470916>
- Kim, H.-S., Chung, Y.-S., & Yoon, M.-B. (2016). An analysis on the impact of large-scale transports of dust pollution on air quality in East Asia as observed in central Korea in 2014. *Air Quality, Atmosphere and Health*, *9*(1), 83–93. <https://doi.org/10.1007/s11869-014-0312-5>
- Kim, H.-S., Huh, J.-B., Hopke, P. K., Holsen, T. M., & Yi, S.-M. (2007). Characteristics of the major chemical constituents of PM_{2.5} and smog events in Seoul, Korea in 2003 and 2004. *Atmospheric Environment*, *41*(32), 6762–6770. <https://doi.org/10.1016/j.atmosenv.2007.04.060>
- Kim, K.-H., & Shon, Z.-H. (2011). Long-term changes in PM₁₀ levels in urban air in relation with air quality control efforts. *Atmospheric Environment*, *45*(19), 3309–3317. <https://doi.org/10.1016/j.atmosenv.2011.03.033>
- Kim, Y., Kim, S.-W., Yoon, S.-C., Kim, M.-H., & Park, K.-H. (2014). Aerosol properties and associated regional meteorology during winter pollution event at Gosan climate observatory, Korea. *Atmospheric Environment*, *85*, 9–17. <https://doi.org/10.1016/j.atmosenv.2013.11.041>
- Kimura, F., & Ohashi, A. (2016). Production networks in East Asia: What we know so far. In *Production Networks and Enterprises in East Asia*, (pp. 33–64). Japan: Springer. Retrieved from http://link.springer.com/chapter/10.1007/978-4-431-55498-1_3
- Koo, Y.-S., Kim, S.-T., Yun, H.-Y., Han, J.-S., Lee, J.-Y., Kim, K.-H., & Jeon, E.-C. (2008). The simulation of aerosol transport over East Asia region. *Atmospheric Research*, *90*(2–4), 264–271. <https://doi.org/10.1016/j.atmosres.2008.03.014>
- KORUS-AQ Science Team (2018). KORUS-AQ Field Campaign Data. <https://doi.org/10.567/Suborbital/KORUSAQ/DATA01>
- Lee, S., Ho, C.-H., Lee, Y. G., Choi, H.-J., & Song, C.-K. (2013). Influence of transboundary air pollutants from China on the high-PM₁₀ episode in Seoul, Korea for the period October 16–20, 2008. *Atmospheric Environment*, *77*, 430–439. <https://doi.org/10.1016/j.atmosenv.2013.05.006>
- Liu, H., Jacob, D. J., Bey, I., Yantosca, R. M., & Duncan, B. N. (2003). Transport pathways for Asian pollution outflow over the Pacific: Interannual and seasonal variations. *Journal of Geophysical Research*, *108*(D20), 8786. <https://doi.org/10.1029/2002JD003102>
- Martins, D. K., Stauffer, R. M., Thompson, A. M., Knepp, T. N., & Pippin, M. (2012). Surface ozone at a coastal suburban site in 2009 and 2010: Relationships to chemical and meteorological processes. *Journal of Geophysical Research*, *117*, D05306. <https://doi.org/10.1029/2011JD016828>
- Newman, S., Jeong, S., Fischer, M. L., Xu, X., Haman, C. L., Lefer, B., et al. (2013). Diurnal tracking of anthropogenic CO₂ emissions in the Los Angeles basin megacity during spring 2010. *Atmospheric Chemistry and Physics*, *13*(8), 4359–4372. <https://doi.org/10.5194/acp-13-4359-2013>
- Oh, H.-R., Ho, C.-H., Kim, J., Chen, D., Lee, S., Choi, Y.-S., et al. (2015). Long-range transport of air pollutants originating in China: A possible major cause of multi-day high-PM₁₀ episodes during cold season in Seoul, Korea. *Atmospheric Environment*, *109*, 23–30. <https://doi.org/10.1016/j.atmosenv.2015.03.005>
- Park, M. H., Kim, Y. P., Kang, C.-H., & Shim, S.-G. (2004). Aerosol composition change between 1992 and 2002 at Gosan, Korea. *Journal of Geophysical Research*, *109*, D19S13. <https://doi.org/10.1029/2003JD004110>
- Popa, M. E., Vollmer, M. K., Jordan, A., Brand, W. A., Pathirana, S. L., Rothe, M., & Röckmann, T. (2014). Vehicle emissions of greenhouse gases and related tracers from a tunnel study: CO: CO₂, N₂O: CO₂, CH₄: CO₂, O₂: CO₂ ratios, and the stable isotopes ¹³C and ¹⁸O in CO₂ and CO. *Atmospheric Chemistry and Physics*, *14*(4), 2105–2123. <https://doi.org/10.5194/acp-14-2105-2014>
- Potosnak, M. J., Wofsy, S. C., Denning, A. S., Conway, T. J., Munger, J. W., & Barnes, D. H. (1999). Influence of biotic exchange and combustion sources on atmospheric CO₂ concentrations in New England from observations at a forest flux tower. *Journal of Geophysical Research*, *104*(D8), 9561–9569. <https://doi.org/10.1029/1999JD900102>
- Sachse, G. W., Collins, J. E. Jr., Hill, G. F., Wade, L. O., Burney, L. G., & Ritter, J. A. (1991). Airborne tunable diode laser sensor for high-precision concentration and flux measurements of carbon monoxide and methane. In H. I. Schiff (Ed.), *Measurement of atmospheric gases, Proceedings of the Meeting*, (Vol. 1433, p. 157). Bellingham, WA: Society of Photo-Optical Instrumentation Engineers. <https://doi.org/10.1117/12.46162>
- Sachse, G. W., Hill, G. F., Wade, L. O., & Perry, M. G. (1987). Fast-response, high-precision carbon monoxide sensor using a tunable diode laser absorption technique. *Journal of Geophysical Research*, *92*(D2), 2071. <https://doi.org/10.1029/JD092iD02p02071>
- Seibert, P., & Frank, A. (2004). Source-receptor matrix calculation with a Lagrangian particle dispersion model in backward mode. *Atmospheric Chemistry and Physics*, *4*(1), 51–63. <https://doi.org/10.5194/acp-4-51-2004>
- Seidel, D. J., Ao, C. O., & Li, K. (2010). Estimating climatological planetary boundary layer heights from radiosonde observations: Comparison of methods and uncertainty analysis. *Journal of Geophysical Research*, *115*, D16113. <https://doi.org/10.1029/2009JD013680>
- Silva, S. J., Arellano, A. F., & Worden, H. M. (2013). Toward anthropogenic combustion emission constraints from space-based analysis of urban CO₂/CO sensitivity. *Geophysical Research Letters*, *40*, 4971–4976. <https://doi.org/10.1002/grl.50954>
- Singer, B. C., & Harley, R. A. (1996). A fuel-based motor vehicle emission inventory. *Journal of the Air & Waste Management Association*, *46*(6), 581–593. <https://doi.org/10.1080/10473289.1996.10467492>
- Staudt, A. C., Jacob, D. J., Logan, J. A., Bachiochi, D., Krishnamurti, T. N., & Sachse, G. W. (2001). Continental sources, transoceanic transport, and interhemispheric exchange of carbon monoxide over the Pacific. *Journal of Geophysical Research*, *106*(D23), 32,571–32,589. <https://doi.org/10.1029/2001JD900078>
- Stohl, A., Forster, C., Frank, A., Seibert, P., & Wotawa, G. (2005). Technical note: The Lagrangian particle dispersion model FLEXPART version 6.2. *Atmospheric Chemistry and Physics*, *5*(9), 2461–2474. <https://doi.org/10.5194/acp-5-2461-2005>
- Stohl, A., Eckhardt, S., Forster, C., James, P., & Spichtinger, N. (2002). On the pathways and timescales of intercontinental air pollution transport: INTERCONTINENTAL AIR POLLUTION TRANSPORT. *Journal of Geophysical Research*, *107*(D23), 4684. <https://doi.org/10.1029/2001JD001396>
- Streets, D. G., & Waldhoff, S. (2000). Present and future emissions of air pollutants in China. *Atmospheric Environment*, *34*(3), 363–374. [https://doi.org/10.1016/S1352-2310\(99\)00167-3](https://doi.org/10.1016/S1352-2310(99)00167-3)
- Streets, D. G., Tsai, N. Y., Akimoto, H., & Oka, K. (2000). Sulfur dioxide emissions in Asia in the period 1985–1997. *Atmospheric Environment*, *34*(26), 4413–4424. [https://doi.org/10.1016/S1352-2310\(00\)00187-4](https://doi.org/10.1016/S1352-2310(00)00187-4)
- Suntharalingam, P., Jacob, D. J., Palmer, P. I., Logan, J. A., Yantosca, R. M., Xiao, Y., & Evans, M. J. (2004). Improved quantification of Chinese carbon fluxes using CO₂/CO correlations in Asian outflow. *Journal of Geophysical Research*, *109*, D18S18. <https://doi.org/10.1029/2003JD004362>
- Tang, W., Arellano, A. F., DiGangi, J. P., Choi, Y., Diskin, G. S., Agustí-Panareda, A., et al. (2018). Evaluating High-Resolution Forecasts of Atmospheric CO and CO₂ from a Global Prediction System during KORUS-AQ Field Campaign. *Atmospheric Chemistry and Physics Discussions*, 1–41. <https://doi.org/10.5194/acp-2018-71>

- Tong, H. Y., Hung, W. T., & Cheung, C. S. (2000). On-road motor vehicle emissions and fuel consumption in urban driving conditions. *Journal of the Air & Waste Management Association*, 50(4), 543–554. <https://doi.org/10.1080/10473289.2000.10464041>
- Turnbull, J. C., Karion, A., Fischer, M. L., Faloona, I., Guilderson, T., Lehman, S. J., et al. (2011). Assessment of fossil fuel carbon dioxide and other anthropogenic trace gas emissions from airborne measurements over Sacramento, California in spring 2009. *Atmospheric Chemistry and Physics*, 11(2), 705–721. <https://doi.org/10.5194/acp-11-705-2011>
- Turnbull, J. C., Tans, P. P., Lehman, S. J., Baker, D., Conway, T. J., Chung, Y. S., et al. (2011). Atmospheric observations of carbon monoxide and fossil fuel CO₂ emissions from East Asia. *Journal of Geophysical Research*, 116, D24306. <https://doi.org/10.1029/2011JD016691>
- van der A, R. J., Mijling, B., Ding, J., Koukouli, M. E., Liu, F., Li, Q., et al. (2017). Cleaning up the air: Effectiveness of air quality policy for SO₂ and NO_x emissions in China. *Atmospheric Chemistry and Physics*, 17(3), 1775–1789. <https://doi.org/10.5194/acp-17-1775-2017>
- Vay, S. A., Choi, Y., Vadrevu, K. P., Blake, D. R., Tyler, S. C., Wisthaler, A., et al. (2011). Patterns of CO₂ and radiocarbon across high northern latitudes during International Polar Year 2008. *Journal of Geophysical Research*, 116, D14301. <https://doi.org/10.1029/2011JD015643>
- Vay, S. A., Woo, J. H., Anderson, B. E., Thornhill, K. L., Blake, D. R., Westberg, D. J., et al. (2003). Influence of regional-scale anthropogenic emissions on CO₂ distributions over the western North Pacific. *Journal of Geophysical Research*, 108(D20), 8801. <https://doi.org/10.1029/2002JD003094>
- Wang, S. X., Zhao, B., Cai, S. Y., Klimont, Z., Nielsen, C. P., Morikawa, T., et al. (2014). Emission trends and mitigation options for air pollutants in East Asia. *Atmospheric Chemistry and Physics*, 14(13), 6571–6603. <https://doi.org/10.5194/acp-14-6571-2014>
- Wang, Y., Munger, J. W., Xu, S., McElroy, M. B., Hao, J., Nielsen, C. P., & Ma, H. (2010). CO₂ and its correlation with CO at a rural site near Beijing: Implications for combustion efficiency in China. *Atmospheric Chemistry and Physics*, 10(18), 8881–8897. <https://doi.org/10.5194/acp-10-8881-2010>
- Ward, D. E., Hao, W. M., Susott, R. A., Babbitt, R. E., Shea, R. W., Kauffman, J. B., & Justice, C. O. (1996). Effect of fuel composition on combustion efficiency and emission factors for African savanna ecosystems. *Journal of Geophysical Research*, 101(D19), 23,569–23,576. <https://doi.org/10.1029/95JD02595>
- Woo, J. H., An, S. M., Kim, D. Y., Kim, H. K., Choi, Y. H., & Kim, Y. H. (2013). *Development of the Asia emission inventory in support of integrated modeling of climate and Air Quality (III)* (No. NIER-SP2013-1). Incheon, Korea: National Institute of Environmental Research.
- Yeon, J.-I., Pyka, A., & Kim, T.-Y. (2016). Structural shift and increasing variety in Korea, 1960–2010: Empirical evidence of the economic development model by the creation of new sectors. *Hohenheim Discussion Papers in Business, Economics and Social Sciences*. Retrieved from <https://www.econstor.eu/handle/10419/146642>
- York, D., Evensen, N. M., Martinez, M. L., & De Basabe Delgado, J. (2004). Unified equations for the slope, intercept, and standard errors of the best straight line. *American Journal of Physics*, 72(3), 367–375. <https://doi.org/10.1119/1.1632486>
- Zhang, Q., Streets, D. G., Carmichael, G. R., He, K. B., Huo, H., Kannari, A., et al. (2009). Asian emissions in 2006 for the NASA INTEX-B mission. *Atmospheric Chemistry and Physics*, 9(14), 5131–5153. <https://doi.org/10.5194/acp-9-5131-2009>
- Zhao, Y., Wang, S., Duan, L., Lei, Y., Cao, P., & Hao, J. (2008). Primary air pollutant emissions of coal-fired power plants in China: Current status and future prediction. *Atmospheric Environment*, 42(36), 8442–8452. <https://doi.org/10.1016/j.atmosenv.2008.08.021>
- Zheng, B., Chevallier, F., Ciais, P., Yin, Y., Deeter, M. N., Worden, H. M., et al. (2018). Rapid decline in carbon monoxide emissions and export from East Asia between years 2005 and 2016. *Environmental Research Letters*, 13(4), 044007. <https://doi.org/10.1088/1748-9326/aab2b3>
- Zhong, Q., Huang, Y., Shen, H., Chen, Y., Chen, H., Huang, T., et al. (2017). Global estimates of carbon monoxide emissions from 1960 to 2013. *Environmental Science and Pollution Research*, 24(1), 864–873. <https://doi.org/10.1007/s11356-016-7896-2>